Growth and Characterization of Tandem-Junction Photovoltaic Nanowires

Hrachowina, Lukas

2022

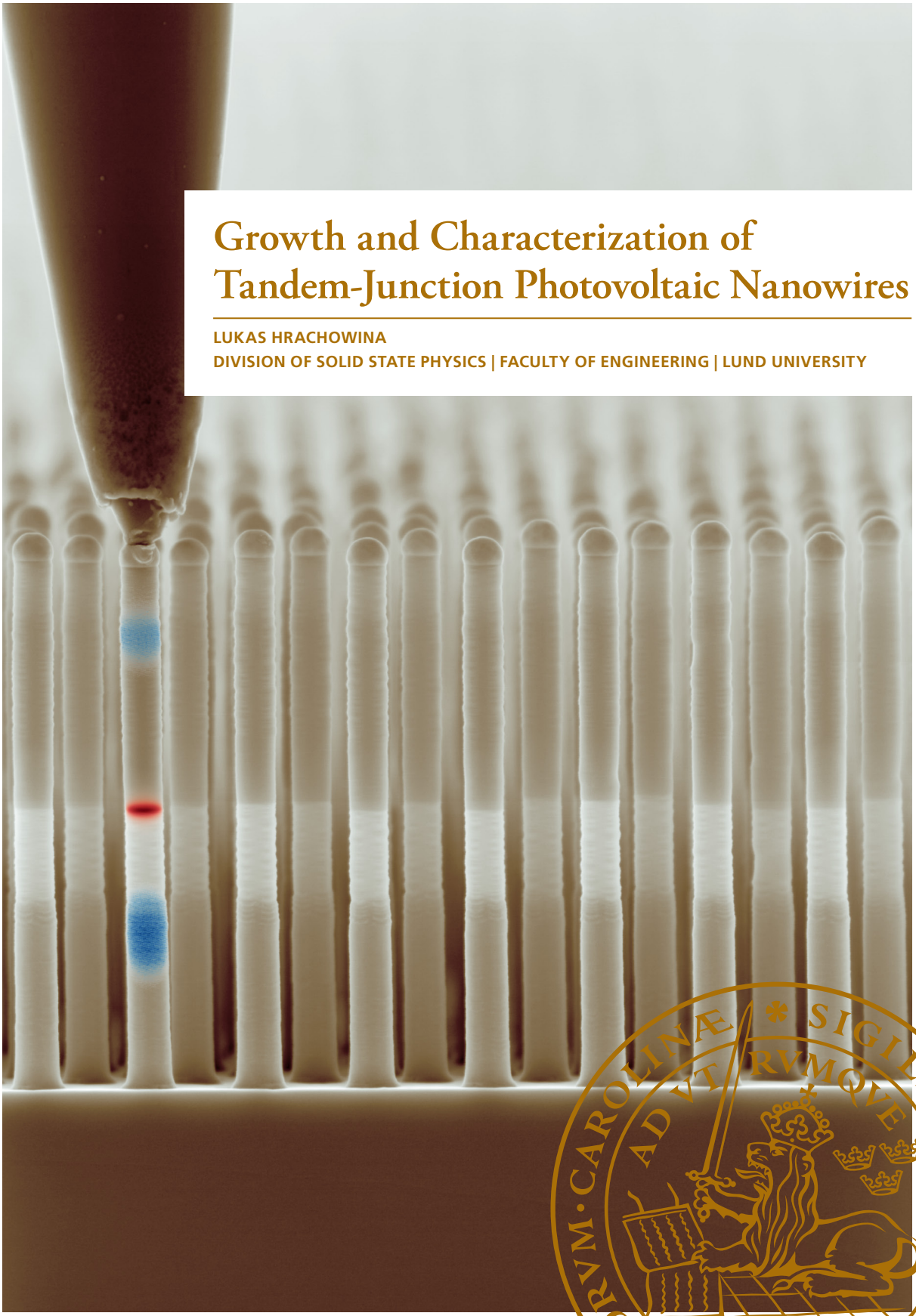

Growth and Characterization of Tandem-Junction Photovoltaic Nanowires

LUKAS HRACHOWINA
DIVISION OF SOLID STATE PHYSICS | FACULTY OF ENGINEERING | LUND UNIVERSITY

Growth and Characterization of Tandem-Junction Photovoltaic Nanowires

Growth and Characterization of Tandem-Junction Photovoltaic Nanowires

Lukas Hrachowina

LUND
UNIVERSITY

DOCTORAL DISSERTATION

by due permission of the Faculty of Engineering, Lund University, Sweden.
To be defended on Wednesday May 25th, 2022, at 13:15 in Rydbergsalen, Sölvegatan 14, Lund, for the degree of Doctor of Philosophy in Engineering.

Faculty opponent
Dr. Esther Alarcón-Lladó

AMOLF, Netherlands

Organization LUND UNIVERSITY	Document name Doctoral Dissertation
	Date of issue 2020-05-25
Author(s) Lukas Hrachowina	Sponsoring organization

Title and subtitle
Growth and Characterization of Tandem-Junction Photovoltaic Nanowires

Abstract

In order to satisfy the growing energy needs of our planet's population, and at the same time mitigate global warming, sustainable energy sources such as solar energy are indispensable. In addition to conventional silicon-based solar cells, nanotechnology offers interesting approaches for complementary applications. Multi-junction solar cells based on III–V semiconductors hold today's world-record efficiencies—twice as efficient as solar cells found on rooftops nowadays—but their high cost is limiting their terrestrial use.

In this thesis, nanowires for photovoltaic applications are studied. Nanowire solar cells have the potential to reach the same efficiencies as the world-record III–V solar cells while only using a fraction of the material. First, InP single-junction nanowires were investigated. For solar energy harvesting, large-area nanowire solar cells have to be processed but so far only devices with less than one mm^2 have been fabricated. To lay the foundation of large-area nanowire solar cells, the wafer-scale synthesis of InP nanowire arrays was systematically studied. Then the effect of embedding InP nanowires in different oxides was investigated. Due to their inherent large surface-to-volume ratio, nanowires require surface passivation. However, fixed charge carriers in the passivating layer can alter the electrostatic potential of nanowires, which was directly imaged by measuring the electron-beam-induced current. Furthermore, the current-voltage characteristics of single nanowires under *in situ* illumination was measured and correlated with electron-beam-induced current measurements, by using a setup that combines a nanoprobe system with an optical fiber coupled to a multi-LED setup inside a scanning electron microscope.

Guided by the multi-LED and electron-beam-induced current setup, tandem-junction nanowires were developed. After identifying and subsequently preventing the occurrence of a parasitic junction when combining an InP n–i–p junction with a tunnel diode, GaInP/InP tandem-junction nanowires were synthesized. An optical and electrical bias was applied to individually measure the electron-beam-induced current of both sub-cells. Finally, axially defined, GaInP/InP/InAsP triple-junction photovoltaic nanowires optimized for light absorption exhibiting an open-circuit voltage of up to 2.37 V were synthesized. The open-circuit voltage amounts to 94 % of the sum of the respective single-junction nanowires. These results pave the way for realizing the next-generation of scalable, high-performance, and ultra-high power-to-weight ratio multi-junction, nanowire-based solar cells.

Key words: III–V semiconductors, nanowire, photovoltaics, tandem junction, MOVPE, EBIC

Classification system and/or index terms (if any)

Supplementary bibliographical information		**Language** English
ISSN and key title		**ISBN** 978-91-8039-209-9 (print) 978-91-8039-210-5 (pdf)
Recipient's notes	**Number of pages:** 179	Price
	Security classification	

Signature  Date 2022-04-12

Growth and Characterization of Tandem-Junction Photovoltaic Nanowires

Lukas Hrachowina

LUND
UNIVERSITY

Front Cover: Scanning electron microscope image of an array of photovoltaic tandem-junction nanowires. One nanowire is electrically contacted by a tungsten nanoprobe. At an applied voltage in forward direction, the electron-beam-induced currents of the two sub-cells of the nanowire (blue) and of the tunnel diode (red) are measured simultaneously with opposite currents.

Faculty of Engineering

Department of Physics, Division of Solid State Physics

ISBN: 978-91-8039-209-9 (print)

ISBN: 978-91-8039-210-5 (pdf)

Printed in Sweden by Media-Tryck, Lund University

Lund 2022

I do not hope, for hoping is a foolish game. I make new lamps and take my measurements. That is the only way to make progress.

— Patrick Rothfuss, The Name of the Wind

Table of Contents

Abstract

In order to satisfy the growing energy needs of our planet's population, and at the same time mitigate global warming, sustainable energy sources such as solar energy are indispensable. In addition to conventional silicon-based solar cells, nanotechnology offers interesting approaches for complementary applications. Multi-junction solar cells based on III–V semiconductors hold today's world-record efficiencies—twice as efficient as solar cells found on rooftops nowadays—but their high cost is limiting their terrestrial use.

In this thesis, nanowires for photovoltaic applications are studied. Nanowire solar cells have the potential to reach the same efficiencies as the world-record III–V solar cells while only using a fraction of the material. First, InP single-junction nanowires were investigated. For solar energy harvesting, large-area nanowire solar cells have to be processed but so far only devices with less than one mm^2 have been fabricated. To lay the foundation of large-area nanowire solar cells, the wafer-scale synthesis of InP nanowire arrays was systematically studied. Then the effect of embedding InP nanowires in different oxides was investigated. Due to their inherent large surface-to-volume ratio, nanowires require surface passivation. However, fixed charge carriers in the passivating layer can alter the electrostatic potential of nanowires, which was directly imaged by measuring the electron-beam-induced current. Furthermore, the current-voltage characteristics of single nanowires under *in situ* illumination was measured and correlated with electron-beam-induced current measurements, by using a setup that combines a nanoprobe system with an optical fiber coupled to a multi-LED setup inside a scanning electron microscope.

Guided by the multi-LED and electron-beam-induced current setup, tandem-junction nanowires were developed. After identifying and subsequently preventing the occurrence of a parasitic junction when combining an InP n–i–p junction with a tunnel diode, GaInP/InP tandem-junction nanowires were synthesized. An optical and electrical bias was applied to individually measure the electron-beam-induced current of both sub-cells. Finally, axially defined, GaInP/InP/InAsP triple-junction photovoltaic nanowires optimized for light absorption exhibiting an open-circuit voltage of up to 2.37 V were synthesized. The open-circuit voltage amounts to 94 % of the sum of the respective single-junction nanowires. These results pave the way for realizing the next-generation of scalable, high-performance, and ultra-high power-to-weight ratio multi-junction, nanowire-based solar cells.

Acknowledgements

Having worked toward this thesis for almost 5 years has been an emotional rollercoaster with many ups, but also downs. Certainly, I could not have accomplished what I have without the help and support of many other people. I am grateful for having had the opportunity to pursue my PhD in Lund. FTF has been a great working environment and NanoLund truly is a great place to do nanoscience.

First, I want to thank my main supervisor, Magnus Borgström. Whenever I knocked on your door, you patiently took the time to discuss experiments even when you were busy yourself. I appreciate that you always found encouraging words that motivated me. I have definitely learned a lot from you. I also want to thank my co-supervisors, Jesper Wallentin and Martin Magnusson. Thank you for your guidance, valuable discussions and advice during study plan meetings.

I have enjoyed working in an international and diverse group. I wish to thank Vilgailė and Xulu, for introducing me to the cleanroom and most importantly the Aixtron 200/4. I am grateful to Gaute, for teaching me how to measure EBIC, which has become an integral part of my experimental work. I am thankful to Enrique, for patiently explaining the physics of solar cells and Yuwei, for processing devices. I also want to thank David A, Kristi, Aditya, Yue, and Matteo for the interesting discussions during group meetings. Patrick, it has been great to work together with you and accompany you during your Master's project.

In addition to having been part of a friendly group, I had the privilege to collaborate with extremely knowledgeable people from other research fields. In particular, I would like to thank Arkady and Xianshao for measuring and explaining time-resolved photoluminescence. I wish to thank Reza, for electroplating, electron-beam-lithography, and all the nice conversations. I want to thank Yang, for countless calculations. Nicklas, unfortunately we only communicated via emails, but I truly learned a lot working together with you. I am thankful to Reine, for measuring TEM. I would like to thank Jesper again—together with Lert and Nils—for the great collaboration and for inviting me to join the experiments at MAX IV. It has been a pleasure to work together with Christelle, Laura and Therese—it is fascinating how you are using nanowires to study cancer cells. Furthermore, I am thankful for the collaboration with Håkan, Mohammad, and Hossein. Although we have not directly

worked together, I would also like to thank Sebastian for discussing various growth-related problems and tools in the cleanroom.

It has been a privilege to work in such a well-equipped cleanroom as Lund Nano Lab. I would like to thank the technical and administrative staff that keep the cleanroom and the division running.

I am glad that I had support from my friends. Thank you Egor for being such a pleasant office mate and becoming a good friend! It has been a great working environment in the exile of FTF in corridor H and I would like to acknowledge the H300-coffee consortium. Especially Sven, Jonatan, Irene, Oskar, and David B have become close friends—thank you for all the good times. I also want to thank all other previous and present PhD students and post-docs for the interestingly absurd conversations during lunch, NanoLund retreats, and after-work beers.

I would like to thank my family, especially my parents, for supporting me to move to Sweden. I am grateful for all the parcels supplying me with sweets from home, and for visiting me here in Lund. Finally, I wish to thank Aleks for always standing by my side and moving to Sweden so that we could be together.

Lukas Hrachowina
Lund, April 2022

Popular Science Summary

In recent decades, the average global surface temperature has increased—an effect that is known as global warming. We have already reached a point of no return at which the melting of glaciers cannot be prevented. The main reason for global warming is the human-induced high emission of greenhouse gases since the industrial revolution. In order to mitigate the effect of global warming, sustainable energy sources need to replace fossil fuels, which are limited but still the primary global energy source.

Solar power is—besides wind and hydropower—one of the most promising ways to generate sustainable energy. Within one hour, the sun supplies the earth with more energy than the global population consumes in an entire year. Solar cells are used to harvest this energy by directly converting sunlight to electricity. Standard solar cells that can be found on rooftops are made from silicon. However, silicon solar cells do not have the highest efficiency of all available solar cell technologies. There are more efficient solar cells based on so-called III–V semiconductors, but they are too expensive to be commonly used terrestrially. Instead, they are mainly used in space applications.

Therefore, there are two factors that need to be considered: the efficiency of a solar cell as well as the cost. Nanowire solar cells promise to reach the high efficiencies of world record solar cells based on III–V semiconductors at a low cost. Nanowires are tiny, elongated structures with a high aspect ratio. Typically, they have a diameter smaller than a few 100 nanometers and a length of a few micrometers. That is roughly a thousand times thinner than a human hair. Thus, nanowires are thinner than the wavelength of visible light, and that causes interesting interactions. For example, nanowires can absorb light from a larger area than their own cross-section. Consequently, an array of nanowires absorbs as much light as a continuous film, even though only 10 % of the area is covered, saving 90 % of the expensive semiconducting materials. In such an array, millions of nanowires are aligned in a periodic pattern and each nanowire acts as a tiny solar cell. Since nanowire solar cells consist of millions of such tiny solar cells, the samples are more forgiving towards defects and it is possible to fabricate flexible devices.

The experimental part of this thesis focuses on the fabrication of such nanowire arrays, as well as on their characterization. First, the pattern of the array is copied from a pre-defined mask or stamp and transferred to a growth substrate using lithography. Then, gold is deposited onto the substrate, following the defined pattern. In a chemical

reactor, molecules containing elements of group III and V are used as precursors and supplied via the gas phase. The gold seeds form an alloy, melt, and then the nanowires start to grow underneath the liquid seed particle. The composition and electric properties of the nanowires can be controlled by using different precursors and adjusting their concentration in the gas phase.

Because nanowires are so small, scanning electron microscopes are often used to investigate them instead of light microscopes. A focused electron beam is scanned over the sample and interacts with the nanowires. One possible interaction is that the focused electron beam kicks out secondary electrons that come from the sample. Those secondary electrons are typically used to image the topography of nanosized samples. Another interaction is the electron-beam-induced current. This effect is similar to the current that is generated by a solar cell upon light illumination but allows for studying solar cells with the spatial resolution of an electron microscope—ideal for photovoltaic nanowires. First, the electron-beam-induced current was used to study single-junction nanowires. Then, guided by electron-beam-induced measurements, nanowires with more than one junction were developed. This lays the foundation for multi-junction—the technology yielding world record solar cell efficiencies—nanowire solar cells.

List of Publications

This thesis is based on the following papers, which will be referred to by their roman numerals in the text.

I **Wafer-Scale Synthesis and Optical Characterization of InP Nanowire Arrays for Solar Cells**
L. Hrachowina, N. Anttu, and M. T. Borgström
Nano Letters **2021,** 21(17), 7347-7353.
I performed displacement talbot lithography (DTL), the nanowire synthesis, and measured the electron-beam-induced current (EBIC) and the optical response. I analyzed the data and was responsible for the writing of the paper.

II **Imaging the influence of oxides on the electrostatic potential of photovoltaic InP nanowires**
L. Hrachowina, X. Zou, Y. Chen, Y. Zhang, E. Barrigón, A. Yartsev, and M. T. Borgström
Nano Research **2021**, 14(11), 4087-4092.
I synthesized the investigated nanowires, deposited the oxides, and measured the EBIC profiles. I analyzed the time-resolved photoluminescence (TRPL) measurements and was responsible for the writing of the paper.

III **Light current-voltage measurements of single, as-grown, nanowire solar cells standing vertically on a substrate**
E. Barrigón, L. Hrachowina, and M. T. Borgström
Nano Energy **2020**, 78, 105191.
I synthesized the InP nanowires and participated in designing the experiments, discussing the results, and writing the paper.

IV **Development and Characterization of Photovoltaic Tandem-Junction Nanowires using Electron–Beam-Induced Current Measurements**
L. Hrachowina, E. Barrigón, and M. T. Borgström
Submitted **2022**.
I developed the synthesis of the nanowires and the biased EBIC measurements. I analyzed the data and was responsible for the writing of the paper.

V **Realization of axially defined GaInP/InP/InAsP triple-junction photovoltaic nanowires for high performance solar cells**
L. Hrachowina, Y. Chen, E. Barrigón, R. Wallenberg, and M. T. Borgström
Submitted **2022**.
I developed the synthesis of the nanowires and performed the single nanowire measurements. I analyzed the data and was responsible for the writing of the paper.

The following publications are not included since they are beyond the scope of this thesis. They are listed in chronological order.

VI **UV exposure: A novel processing method to fabricate nanowire solar cells**
Y. Zhang, Y. Chen, L. Hrachowina, C. Sundvall, I. Åberg, and M.T. Borgström
2019 46th IEEE Photovoltaic Specialists Conference, **2019**, 2646-2648, 8980764.

VII **Nanoprobe-Enabled Electron Beam Induced Current Measurements on III-V Nanowire-Based Solar Cells**
E. Barrigón, G. Otnes, Y. Chen, Y. Zhang, L. Hrachowina, X. Zeng, L. Samuelson, and M.T. Borgström
2019 46th IEEE Photovoltaic Specialists Conference, **2019**, 2730-2733, 8980491.

VIII **Unravelling processing issues of nanowire-based solar cell arrays by use of electron beam induced current measurements**
E. Barrigón, Y. Zhang, L. Hrachowina, G. Otnes, and M.T. Borgström
Nano Energy **2020**, 71, 104575.

IX **Photovoltaic nanowires affect human lung cell proliferation under illumination conditions**
T.B. Olsson, L. Abariute, L. Hrachowina, E. Barrigón, D. Volpati, S. Limpert, G. Otnes, M.T. Borgström, and C.N. Prinz
Nanoscale **2020**, 12(26), 14237-1424.

X **Self-Limiting Polymer Exposure for Vertical Processing of Semiconductor Nanowire-Based Flexible Electronics**
Y. Zhang, L. Hrachowina, E. Barrigón, I. Åberg, and M.T. Borgström
ACS Applied Nano Materials **2020**, 3(8), 7743-7749.

XI **Development and Characterization of a bottom-up InP Nanowire Solar Cell with 16.7% Efficiency**
L. Hrachowina, Y. Zhang, A. Saxena, G. Siefer, E. Barrigón, and M.T. Borgström
2020 47th IEEE Photovoltaic Specialists Conference, **2019**, 2646-2648, 8980764.

XII **Direct Three-Dimensional Imaging of an X-ray Nanofocus Using a Single 60 nm Diameter Nanowire Device**
L. Chayanun, L. Hrachowina, A. Björling, M.T. Borgström, and J. Wallentin
Nano Letters **2020**, 20(11), 8326-8331.

XIII **Comparison of Triethylgallium and Trimethylgallium Precursors for GaInP Nanowire Growth**
D. Alcer, A.P. Saxena, L. Hrachowina, X. Zou, A. Yartsev, and M.T. Borgström
Physica Status Solidi (B) Basic Research **2021**, 258(2), 2000400.

XIV **Gain and bandwidth of InP nanowire array photodetectors with embedded photogated InAsP quantum discs**
H. Jeddi, M. Karimi, B. Witzigmann, X. Zeng, L. Hrachowina, M.T. Borgström, and H. Pettersson
Nanoscale **2021**, **13**(12), 6227-6233.

XV **Semiconductor nanowire array for transparent photovoltaic applications**
Y. Chen, L. Hrachowina, E. Barrigón, J. P. Beech, D. Alcer, R. Lyttleton, J. R. Jam, L. Samuelson, H. Linke, and M. T. Borgström
Applied Physics Letters **2021**, 118(19), 191107.

1 Introduction

1.1 Motivation

The growing population of our planet has an increasing demand for energy [1]. Fossil fuels such as coal, petroleum, and natural gas are still the primary global energy source [2], even though they are limited and cause severe environmental damage [3]. Sustainable energy sources are indispensable to reduce global warming according to the Paris Agreement.

Solar power, as well as wind power and hydropower, is an important way to generate renewable, practically unlimited energy. Within one hour, the sun supplies our planet with energy sufficient for humanity's yearly energy consumption [4]. Photovoltaic cells are used to convert sunlight directly into electricity. Most often, silicon is used, which is earth abundant and cheap in comparison with other semiconductors. However, although silicon has several advantages, the world record solar cells depend on III–V semiconductors, which are composed of atoms from the third and fifth group of the periodic table of the elements. One reason, besides the indirect band gap of silicon, is that one material by itself cannot efficiently convert the full solar spectrum into electricity. Some wavelengths do not have sufficient energy to excite the electrons of the semiconductor—those wavelengths are simply not absorbed—and others have too much energy, for which the excess energy is lost as heat due to thermalization. These two are the major fundamental loss processes in single-junction solar cells. Therefore, to increase the efficiency of a solar cell, several different materials are combined. The world record solar cell combines six different III–V semiconductors [5]. This technology is called multi-junction solar cells. However, especially the group III elements, such as gallium and indium, are scarce and expensive. The high cost of multi-junction solar cells, including the chemical precursors, growth substrate and machines needed for fabrication [6], is the main reason that they are not used in large area terrestrial applications.

In order to produce sufficient energy based on solar power, large areas have to be utilized to harvest light. In addition to traditional solar cells that can be placed on rooftops or arranged in solar power plants, semi-transparent solar cells are interesting, as they can be used in building-integrated photovoltaics [7]. While semi-transparent solar cells

have an inherently lower efficiency than standard solar cells, their prospect is that they could be used to generate power from additional surfaces, such as windows or displays.

It is therefore of interest to find materials that can be used to fabricate cheap solar cells that have either a high efficiency or can be used in semi-transparent applications. Besides other emerging technologies such as dye-sensitized solar cells [8, 9] and perovskites [10, 11], nanowire photovoltaics promise to reach the high efficiencies of III–V multi-junction technology by using only a fraction of the necessary material [12-15]. Furthermore, by adjusting the distance between nanowires, the transparency can be fine-tuned.

1.2 Nanowires

Nanowires are structures confined to the nanoscale in two dimensions with a high aspect ratio [16-19]. Typically, they are thinner than 100 nm and several micrometers long. Depending on the time of publication, shape, or application, sometimes different names are found. Especially in the initial stage, such structures were often referred to as whiskers [20-25]. Sometimes the term nanorods is used, typically if the described structures do not have a very high aspect ratio. Nanowires are commonly referred to as 1-dimensional (1D) structures [26-28], a term most often used to describe the elongated shape of nanowires. However, depending on the material, for small enough diameters it is possible to be in the range of, or smaller than, the Debye length. In such cases, it is even reasonable to speak of 1D in the sense of electronic properties and the structures can be referred to as quantum wires. Figure 1.1 illustrates different 1D nanostructures [28].

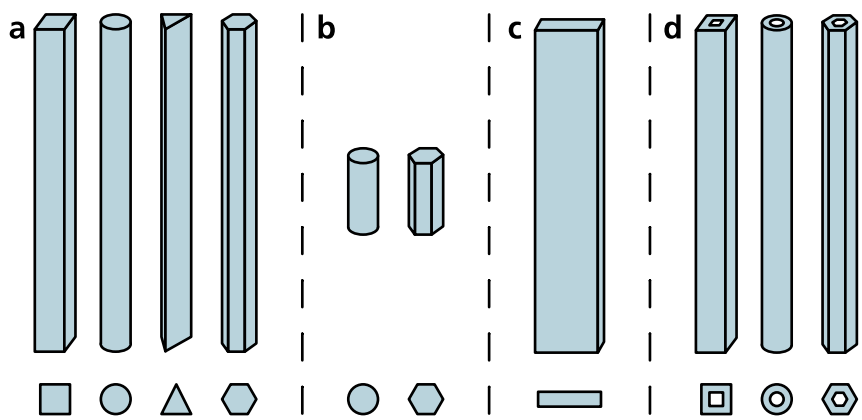

Figure 1.1: Different elongated nanostructures: (a) Typical nanowire geometries with different cross-sections. (b) Shorter structures are often called nanorods. (c) Broad structures are referred to as nanobelts. (d) In contrast to nanowires, nanotubes are hollow. Adapted with permission from [28]. © 2010 Elsevier Ltd.

The nanowire geometry enables novel material designs. Possible heterostructures include axial segments of different materials [25], core-shell structures [29], or side branches [30]. In recent years, interconnected nanowires in two dimensions raised attention for their possible applications in quantum computing [31]. With direct writing methods such as focused-electron-beam-induced deposition, it is even possible to synthesize interconnected nanowire networks in three dimensions [32]. In Figure 1.2 some possible nanowire heterostructures are shown.

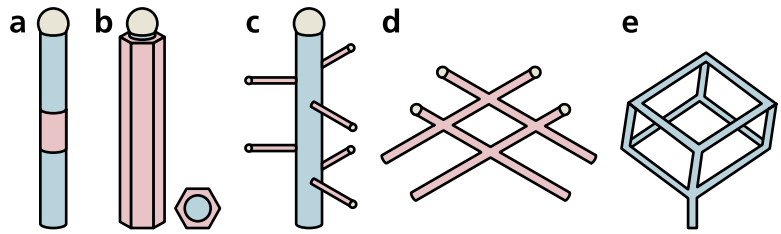

Figure 1.2: Possible bottom-up synthesized nanostructure geometries: (a) Axial heterostructures. (b) Radial heterostructures. (c) Branched nanowires. (d) 2D interconnected nanowires. (e) 3D interconnected nanowires.

Due to their nano-scaled size, nanowires have a high surface-to-volume ratio. Because of that, one possible application are gas sensors that detect the change of resistivity of the material after adsorption of certain analytes [33]. Other promising applications do not rely on the advantageous physical properties of nanowires compared to bulk materials but on the arising possibilities from their geometry for device integration. For example, nanowires can be embedded in flexible polymers to harvest mechanical energy from piezoelectric [34] and triboelectric effects [35].

1.3 Outline

This thesis focuses on the synthesis and characterization of photovoltaic nanowires and is based on five papers. Papers I-III study single-junction nanowires. In Paper I, the feasibility to synthesize nanowire arrays on a large area is demonstrated, which is necessary for photovoltaic applications. Paper II addresses the surface passivation of nanowires. Paper III introduces a multi-LED setup that is used to characterize single nanowires. Papers IV and V describe the development of multi-junction nanowires. In Paper IV, electron-beam-induced current is used in combination with the multi-LED setup to develop photovoltaic dual-junction nanowires and characterize their sub-cells. In Paper V the technology is extended to photovoltaic triple-junction nanowires. In order to introduce the research papers, the first part of this thesis is supposed to give a general overview of the concepts and methods relevant for the publications and ends with a summary of the experimental results and an outlook for future work.

2 Nanowire Synthesis

Strategies to synthesize nanostructures can be categorized into two approaches: top-down and bottom-up [36]. Top-down processing starts from a bulk material that is reduced in size by milling or etching. In order to produce nanowires this way, *e.g.*, nanoparticles can be used as protection against an anisotropic etching method, such as reactive ion etching [37]. The advantage of top-down approaches is that these processes are typically scaled up easily. On the other hand, top-down approaches are limited to the bulk material that is used as a starting point. In this regard, bottom-up synthesis is much more flexible. The idea is to start from molecular precursors that are combined to build the desired material. With this approach it is possible to create heterostructures that would not be accessible by top-down approaches, such as core-shell, or branched nanowires. Even though axial heterostructures could be produced by top-down processes, bottom-up syntheses of nanowires enable the combination of lattice mismatched materials because strain can be relaxed in radial direction [38]. Even though it is possible to manually move and position single atoms [39], it would take too much time to synthesize materials this way. In epitaxy, a crystalline growth substrate is used as a template to determine the atomic positions of a new crystal.

The epitaxial growth of crystals can be achieved by different techniques, classified by the phase that supplies the constituent atoms of the crystal. Solid-phase epitaxy (SPE) describes the crystallization of an amorphous solid [40]. In liquid-phase epitaxy (LPE), a crystal grows at the interface between a supersaturated solution or melt and a growth substrate [41]. Similarly, in vapor-phase epitaxy (VPE) the constituents of the crystal are supplied via the gas phase. This can be achieved by both physical vapor deposition (PVD) techniques, such as MBE [42] and pulsed laser deposition [43], or by chemical vapor deposition (CVD) techniques [44].

Although the principle for many techniques is similar, namely providing precursors to the reaction front, they differ in important variables such as pressure and precursor chemistry [45]. For CVD processes molecular precursors with sufficiently high vapor pressures are used that are introduced as gases into the reaction chamber. There, the molecules need to thermally dissociate, and choosing a suitable precursor is crucial as to, *e.g.*, avoid impurity incorporations. For MBE processes on the other hand, usually elementary sources are used at ultra-high vacuum to bombard the surface with atoms. As a result, MBE synthesized crystals are of very high purity—though some CVD techniques have already caught up—and atomically sharp interfaces can be achieved.

On the other hand, the ultra-high vacuum requirements and low throughput of MBE result in a high cost.

Metalorganic vapor phase epitaxy (MOVPE—also referred to as OMVPE, MOCVD, or OMCVD [46]) is a subcategory of CVD processes that is commonly used to grow epitaxial crystals of III–V semiconductors. Compared to MBE, the reactor design is relatively simple, and a high throughput can be achieved. MOVPE is a mature technique that yields high purity crystals and is used industrially because uniform samples can be produced on a large scale.

2.1 Metalorganic Vapor-Phase Epitaxy

In MOVPE, metalorganic precursors are supplied as a vapor to grow epitaxial crystals. In order to synthesize III–V semiconductors, precursors from both group III and V of the periodic table of elements are used. Typically, the alkyl compounds of group III elements and hydrides of the group V elements are used. While the gaseous group V hydrides such as phosphine (preferred IUPAC name: phosphane, PH_3) and arsine (preferred IUPAC name: arsane, AsH_3) are stored liquefied in high-pressure gas bottles, the group III precursors are typically liquid and stored in temperature-controlled bubblers. Typical examples of liquid group III precursors include trimethylgallium (TMGa), triethylgallium (TEGa), trimethylaluminium (TMAl), and triethylindium (TEIn), while trimethylindium (TMIn) is a solid. In addition to being highly corrosive, the reagents are flammable and will burn on contact with air [47]. All of these are Lewis acids since one p-orbital remains empty after sp^2 hybridization and acts as electron acceptor. At the same time, the group V precursors have a lone pair of valence electrons and act as Lewis bases. Figure 2.1 illustrates the trigonal planar molecular geometry of group III precursors with an empty p-orbital and the tetrahedral molecular geometry of group V precursors with an electron lone pair. A reaction between Lewis acid and base leads to adduct formation. Attempts at using such adducts as single-source precursors posed problems due to their inherently low vapor pressure [48]. Instead, it is more feasible to let the precursors react at elevated temperatures in the growth chamber. A general chemical reaction can be written in the form of: $A_{III}(C_xH_{2x+1})_3 + B_VH_3 \rightarrow A_{III}B_V + 3\ C_xH_{2x+2}$, where A_{III} and B_V are atoms of group III and V, respectively, and C_xH_{2x+1} a generalized acyclic alkyl group. However, the process is complex and in reality, many elementary reactions need to be considered.

Once introduced into the growth chamber, the precursors may undergo different reaction routes, as schematically drawn in Figure 2.2. First, due to the elevated temperature in the growth chamber, the precursors might pyrolyze homogeneously in the gas phase to form intermediate reactants. Unintended side reactions between the precursors can already occur in the gas phase. In the reaction chamber there is a gradient

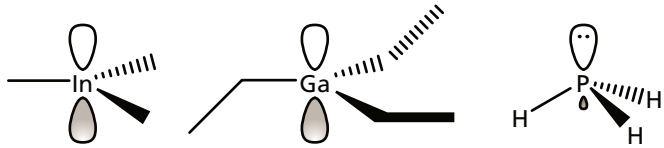

Figure 2.1: Example precursors for III–V semiconductor synthesis. Group III precursors such as trimethylindium and triethylgallium are sp^2-hybridized and have an empty p-orbital that can accept electrons. Group V precursors such as phosphine are sp^3-hypridized and have one lone pair of electrons, indicated by two dots.

in the gas flow—due to the viscosity of the gas phase—resulting in a reduced velocity at the substrate, a temperature gradient, especially for cold-wall reactors, and a concentration gradient of the precursors. Therefore, to arrive at the growth substrate, the precursors and intermediate reactants need to diffuse through a boundary layer. At the surface, the adsorbed precursors pyrolyze heterogeneously to intermediate reactants. The adsorbed reactants diffuse along the surface until they are either incorporated in a growing nucleus or desorb back to the gas phase and are ultimately removed from the growth chamber to the exhaust by a pump.

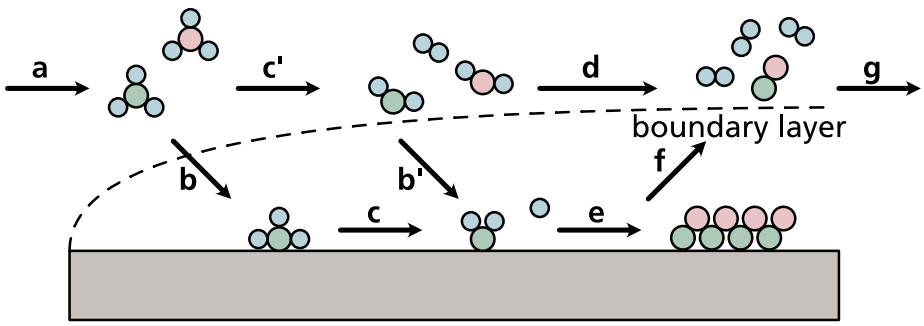

Figure 2.2: Possible reaction routes of precursors in the reaction chamber. (a) Transport of the precursors in the growth chamber. (b) Diffusion of the precursors (b′ intermediate species) through a boundary layer and adsorption to the substrate. (c) Heterogeneous (c′ homogeneous) pyrolysis of the precursors. (d) Gas-phase reactions might lead to powder formation. (e) Diffusion of adatoms to a nucleus and subsequent crystallization. (f) Desorption of by-products. (g) The by-products and unreacted precursors are removed from the growth chamber by a pump. Adapted with permission from [49]. © 2021 Springer Nature Limited.

The growth rate depends on the temperature and three growth regimes can be distinguished (see Figure 2.3). At low temperatures, the growth is limited by the reaction kinetics of the precursors which results in an exponential dependance on the temperature. At an intermediate temperature, the growth rate is limited by the mass transport of the precursors to the growth substrate and almost independent of the temperature. At even higher temperatures, the growth rate is decreasing because of desorption of the reactants.

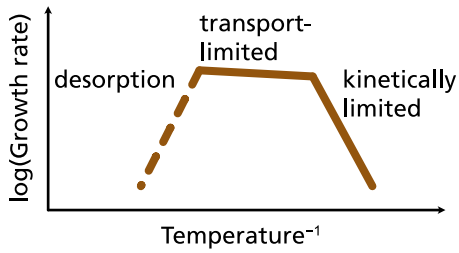

Figure 2.3: Logarithmic growth rate as a function of inverse temperature.

Epitaxial nanowire growth follows the same growth modes as thin films, just on a smaller scale. The growth mode of the deposit depends on the surface free energies of the substrate and the growing crystal nucleus. If the surface free energy of the substrate is equal or larger than the sum of the surface energy of the nucleus and the interface free energy of the substrate and nucleus, layer-by-layer growth (Frank van der Merwe mode [50-52], Figure 2.4a) occurs. On the other hand, if the interface free energy of the substrate and nucleus is larger than the sum of the surface free energies of the substrate and the nucleus, the deposit tends to form islands (Volmer–Weber mode [53], Figure 2.4b). An intermediate growth mode—the Stranski–Krastanov mode [54], Figure 2.4c—is possible as well. In this case, first a wetting layer is formed. At a critical thickness, solid diffusion from the wetting layer leads to island growth [55, 56].

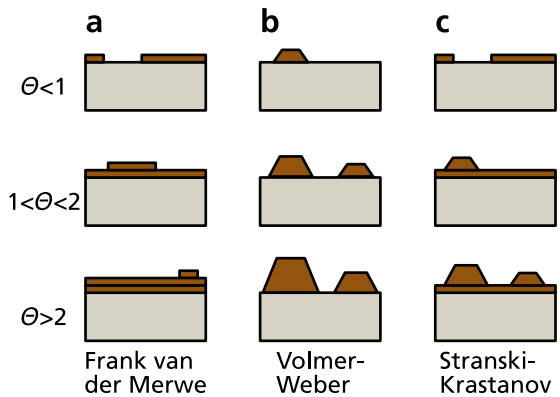

Figure 2.4: Thin film growth modes with increasing surface coverage Θ over time. (a) Frank van der Merwe layer-by-layer mode. (b) Volmer–Weber island growth. (c) Stranski–Krastanov layer plus island growth.

Figure 2.5 shows a simplified schematic of the MOCVD reactor that was used for the experimental work of this thesis, an Aixtron 200/4. The sample is placed on top of a graphite susceptor which is heated by infrared lamps. During crystal growth, the

substrate carrier is rotated by a gas flow. Precursors are stored either in gas tanks or in temperature-controlled bubblers and transported via a carrier gas (hydrogen, H_2) to the reaction chamber. Mass flow controllers (MFC) are used to control the precursor flux. The reaction chamber has a purged viewport for *in situ* optical reflectometry. A scrubber is used to filter toxic waste from the exhaust gas.

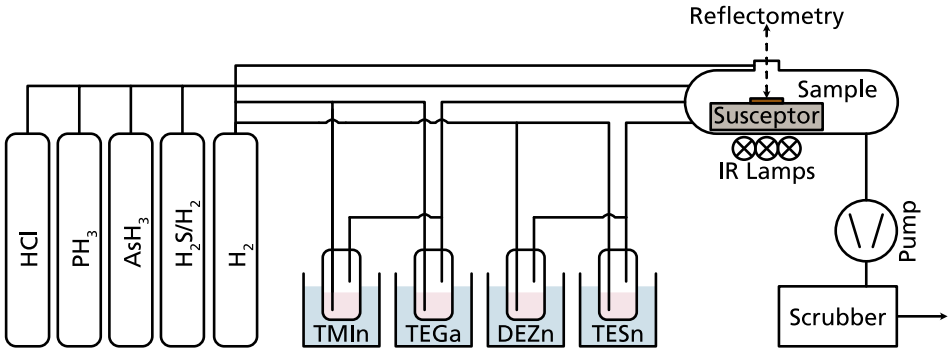

Figure 2.5: Simplified schematics of an Aixtron 200/4 MOVPE reactor. The gaseous hydrides are stored in high-pressure gas bottles and the metalorganic precursors are stored in temperature-controlled bubblers. Different lines are available for hydrides, group III precursors, and dopants to prevent intermixing before arriving at the growth chamber.

2.1.1 Bubbler Cylinders

While the group V hydrides are gaseous, the metalorganic group III compounds are typically liquid or solid. In order to be used as a precursor in MOVPE, bubbler cylinders are used. The bubbler cylinder is a container made of stainless steel with an input and an output tube. A flow of the carrier gas, typically H_2, is led through the input tube. In the case of liquid precursors, this leads to the carrier gas being bubbled through the liquid. For solid precursors, the gas flow permeates a fine powder. The precursor evaporates, or sublimes, and is transported with the carrier gas into the reaction chamber.

Especially for liquid precursors, this setup leads to a controlled and reproducible precursor flow. The precursor flux depends on the vapor pressure P_{vap} of the compound. Typically, a simplified version of the semi-empirical Antoine equation, with two parameters a and b, the August equation, is used. The parameters for most available precursors can be found in tables, however, they are typically listed in units of mmHg.

$$P_{\text{vap}} = 10^{a-\frac{b}{T}} \tag{2.1}$$

The vapor pressure is dependent on the temperature T of the precursor in the bubbler which is controlled by thermoelectric chillers. The volumetric flux of the metalorganic precursor $\Phi_{V,MO}$ flowing out of the bubbler depends on the input carrier gas flux Φ_{V,H_2} that is controlled by a MFC, on P_{vap}, and on the total pressure in the bubbler P_{tot}.

$$\Phi_{V,MO} = \frac{P_{vap}}{P_{tot} - P_{vap}} \cdot \Phi_{V,H_2} \tag{2.2}$$

The molar flux of the metalorganic precursor $\Phi_{M,MO}$ is simply obtained by dividing $\Phi_{V,MO}$ by the molar volume (22.4 l/mol), and the molar fraction of the metalorganic precursor χ_{MO} is obtained by dividing $\Phi_{V,MO}$ by the total flow entering the reaction chamber.

2.1.2 Epison

While the liquid precursors have a constant vapor pressure and the bubbler cylinders therefore generate a stable $\Phi_{M,MO}$, solid precursors are prone to instabilities. As long as the carrier gas flows through a homogeneous powder bed, $\Phi_{M,MO}$ should be stable. However, over time, channels through the solid TMIn can occur, resulting in a reduced interaction time and surface between the solid precursor and the carrier gas.

To monitor $\Phi_{M,MO}$, EPISON® gas concentration sensors are used. The EPISON® sensor measures the speed of sound in a binary gas mixture, H_2 and the metalorganic precursor, and once calibrated, this can be used to measure the concentration. The EPISON® sensor is set in a feedback loop and sends a signal to the MOVPE reactor to automatically adjust Φ_{V,H_2} to achieve the desired $\Phi_{M,MO}$. Thereby it is possible to compensate for variations of the vapor pressure, enabling the sublimation of solid precursors such as TMIn in a reproducible manner.

2.1.3 Laytec

To ensure successful and reproducible experiments, it is important to have *in situ* control inside the growth chamber. One method that is compatible with the higher pressures of MOCVD is optical reflectometry [57, 58]. This tool, which is commonly used to characterize layer growth, can be adapted to measure the nanowire length, and even diameter, with high temporal resolution *in situ*, in real time [59]. The incoming light is reflected at the top of the nanowires but also at the substrate, which leads to wavelength λ dependent interference maxima and minima. The length L of nanowires can then be calculated from the number of maxima m according to equation (2.3). The effective refractive index n_{eff} needs to be measured for different pattern periodicities.

$$L = \frac{m\lambda}{2n_{\text{eff}}} \tag{2.3}$$

Figure 2.6a shows the measured 2D reflectance plot of a nanowire sample grown with MOVPE over time and Figure 2.6b shows the reflectance for a selected wavelength. At 250 s the reflectivity of the substrate increases during the high temperature anneal that is used to desorb surface oxides. After 10 min, the temperature is decreased to the growth temperature and then the group III precursor is introduced into the reactor. The growth of nanowires is indicated by oscillations in the reflectance.

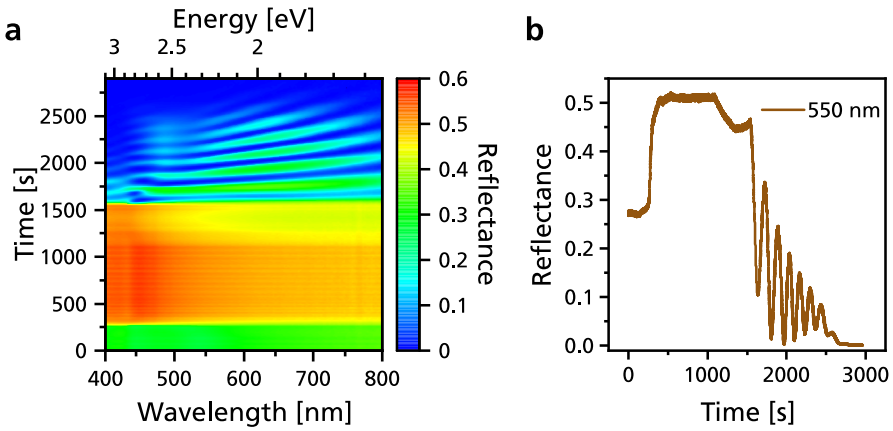

Figure 2.6: (a) Reflectance plot of nanowires after growth. (b) Reflectance signal at the selected wavelength of 550 nm.

2.1.3.1 Ex Situ Reflectometry

While *in situ* reflectometry is a useful tool to control the nanowire length during synthesis, the measurement is limited to a small spot at the center of the growth substrate. *Ex situ* reflectometry has the advantage that the entire sample can be investigated. However, *in situ* reflectometry is based on tracking and counting the oscillations of the reflection that appear due to the change in interference while the nanowires are growing, and this is not possible *ex situ*. On the other hand, after synthesis, it is possible to measure the reflectance with a much higher signal-to-noise ratio. By modelling the reflectance of a nanowire array depending on the length L and diameter D of the nanowires, a reflectance database can be generated. Then, by comparing the measured reflectance to the database and using a global fitting, it is possible to simultaneously obtain L and D [60]. Using this approach, large area nanowire arrays were investigated fast and automatized in a conventional photoluminescence mapper in Paper I.

2.2 Vapor–Liquid–Solid Mechanism

In order to grow nanowires, crystal growth has to occur anisotropically along a specific crystal direction. Some crystals prefer to grow in one direction naturally, due to an anisotropic crystal structure [26]. Most materials do not show this behavior and some further assistance is necessary to grow nanowires.

One pioneering result was already reported in the 1960s, when Wagner and Ellis described Au droplet induced whisker growth on silicon which they termed vapor–liquid–solid (VLS) growth [21].

Au and Si form a eutectic system. Figure 2.7a shows a schematic phase diagram of a eutectic system and highlights five relevant points (i-iii') at an arbitrary temperature. As can be seen in the measured Au-Si phase diagram (Figure 2.7b), pure Au has a melting temperature of 1064 °C. Therefore, at typical growth temperatures, Au is still solid. Figure 2.7c depicts the VLS mechanism, referring to the compositions in Figure 2.7a. When pure Au (i) is heated to typical growth temperatures, it is still solid. If Si is supplied to the Au seed—via the gas phase, or the growth substrate—Si is dissolved in Au which reduces the melting point. At a sufficient Si concentration (ii), the solid seed starts to melt and is in equilibrium with a liquid phase with concentration (ii'). If further Si is supplied, the seed completely melts. Only then can the Si concentration in the seed be further increased until supersaturation in the liquid is reached (iii), followed by precipitation of crystalline Si underneath the Au-Si droplet. The purity of the Si crystal, the nanowire, is given by the phase diagram and is limited by the solubility of Au in Si at the growth temperature (iii'). The incorporation of Au can be problematic due to the formation of deep traps [61]. According to the measured Au-Si phase diagram (Figure 2.7b) the Au incorporation should be negligible. However, Au has been detected in VLS grown Si nanowires [62, 63] at levels of ~1×10^{16} atoms/cm^3. Nevertheless, in most cases the nanowire surface is the limiting factor for device performance [62].

During VLS growth of a nanowire, nucleation typically occurs at the triple phase boundary, corresponding to position (1) in Figure 2.7c. Other nucleation sites are at the nanowire side facets (position 2) and on the substrate (position 3) via vapor–solid (VS) growth. By increasing the growth temperature, the main growth mode can be switched from VLS to VS in order to grow, *e.g.*, radial heterostructures such as p–n junctions or a passivating shell.

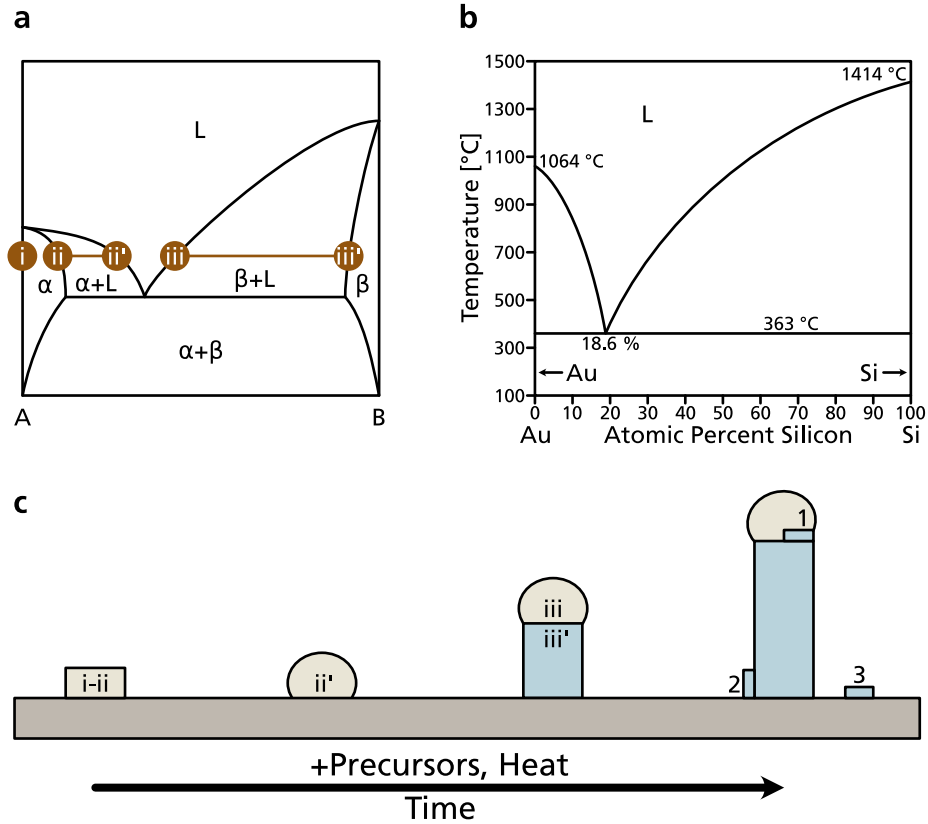

Figure 2.7: (a) Schematic binary, eutectic phase diagram. Five compositions relevant for the VLS mechanism are highlighted. (b) Si-Au phase diagram. Si and Au form a eutectic that melts already at 363 °C at the eutectic composition of $Au_{0.81}Si_{0.19}$. Adapted with permission from [64]. © 1983 Springer. (c) Schematic of the steps involved in nanowire growth via the VLS mechanism, referring to the composition from (a). In addition to nucleation at the triple phase boundary (1), VS growth at the nanowire sidewall (2) and the substrate (3) are possible.

The VLS mechanism is still used to grow nanowires and has been proven to be versatile with respect to both the nanowire and seed material. Similar approaches work even with solid (S) particles, in solutions (S) or supercritical fluids (SF) and many different acronyms such as VSS [65], SLS [66], SSS [67], SFLS [68], SFSS [69] have been introduced to describe nanowire growth in various environments. All of them have in common that precursors are supplied by a fluid phase and accumulate in a seed particle until supersaturation is achieved and a solid nanowire grows.

In order to investigate the growth mode of nanowires, *in situ* transmission electron microscopes have been used [70, 71]. These studies have verified both VLS and VSS mechanisms [72] but also complex interactions with ledge flows [73] and truncated growth facets [74].

Another way to grow nanowires is to use selective area epitaxy [75]. For this, an inert growth mask, typically SiO_2 or Si_3N_4, is defined by lithography. By selecting the right growth conditions, anisotropic crystal growth can lead to untapered nanowires after growth.

2.3 III–V Nanowires

While bulk III–V semiconductors (with the exception of nitrides) are only accessible in the zincblende crystal structure, in nanowires another polytype can be synthesized, the wurtzite crystal structure. The zincblende and wurtzite structure have similar close-packed planes (in [111] and [0001] direction, respectively), that only differ in the stacking sequence (Figure 2.8a) [76]. The cubic zincblende structure is represented by a proceeding stacking of three different close-packed planes, ABC, while the hexagonal wurtzite structure is a repetition of only two different planes, AB. Figure 2.8b shows a drawing of an InP nanowire with a zincblende segment embedded in two wurtzite segments. The atomic arrangement was determined by high resolution TEM [77]. In Figure 2.8c a zincblende nanowire is drawn, for which twinning superlattices can be observed [78]. The crystal structure of VLS grown III–V nanowires can be controlled by changing the involved surface energies during growth that define the contact angle of the liquid seed droplet [79-85]. The contact angle of the seed particle—and consequently the crystal structure—is also affected by doping [78, 86, 87].

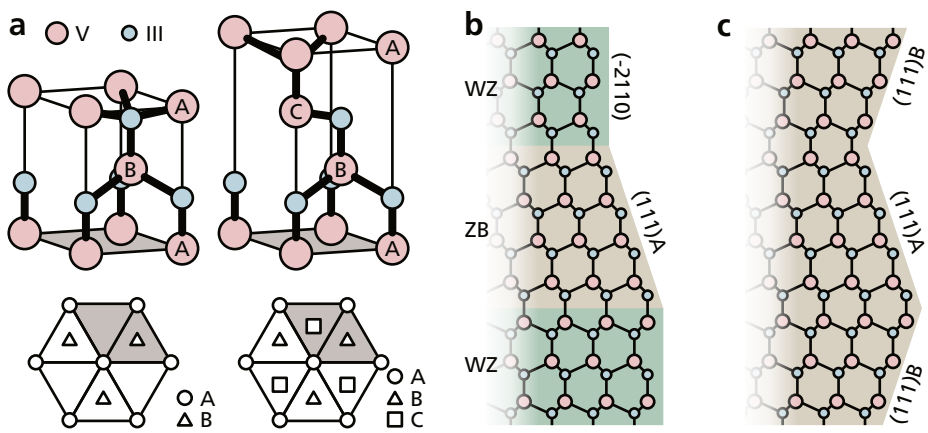

Figure 2.8: (a) Crystal structures of wurtzite (left) and zincblende (right) in 3D geometry (top) and 2D projection (bottom). Adapted with permission from [76]. © 1992 American Physical Society. (b) Atomic arrangement in zincblende and wurtzite InP determined by high resolution TEM. Adapted with permission from [77]. © 1992 American Chemical Society. (c) In pure zincblende nanowires twinning superlattices can be observed.

In contrast to group IV semiconductors, most III–V semiconductors have a direct bandgap for both cubic and hexagonal crystal structures, with only a small offset. Exceptions are GaP and Al–B_V semiconductors that have an indirect band gap in the zincblende crystal structure, but a direct band gap in the wurtzite crystal structure [88]. Therefore, III–V semiconductors are used in many optoelectronic applications. In Figure 2.9 the difference between the direct band gap of InP compared to the indirect band gap of Si is illustrated. To excite electrons from the valence to the conduction band, only a photon is needed for a direct band gap, but for an indirect band gap an additional phonon is required to enable the change in momentum.

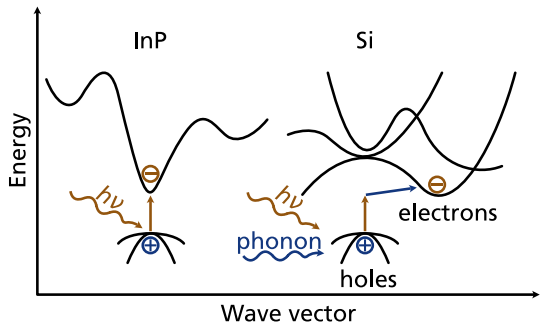

Figure 2.9: A sketch of the comparison between the direct bandgap of InP and the indirect bandgap of silicon.

For many optoelectronic applications, absorption and emission of a specific wavelength is desired. Solid solutions of the binary III–V semiconductors can be synthesized to adjust the band gap of the semiconductor material. Ternary solid solutions consist of two III–V semiconductors with a shared group III or group V element. By changing the composition, the desired band gap can be achieved. However, according to Vegard's law, the lattice constant will change as well. The resulting lattice mismatch will lead to defects during crystal growth of thin films, once again limiting the number of available materials that can be combined. Quaternary solid solutions of III–V semiconductors even use four different elements. This enables the adjustment of the band gap for a given lattice constant. However, the complexity of maintaining control over the material's composition and quality increases dramatically. One major advantage of nanowires is that strain can be released in radial direction. Thus, below a critical diameter, lattice mismatched materials can be grown epitaxially along the nanowire axis without inducing defects [89].

2.3.1 Indium Phosphide

InP is a binary III–V semiconductor that is manufactured as single-crystalline boules which are cut into wafers by a liquid phosphorus encapsulated Czrochalski

method [90]. Due to its direct band gap and excellent optoelectronic properties, InP is used in photovoltaics, lasers, LEDs, and high-speed electronics. The only known crystal structure for bulk InP is cubic zincblende with a direct band gap of 1.34 eV at room temperature.

The first reports of InP nanowires were based on laser-assisted catalytic growth [91-93] in which the laser ablation of an $InP_{0.95}Au_{0.05}$ target was combined with the VLS mechanism. Soon afterwards, epitaxial InP nanowires where synthesized using TMIn and *tert*-butylphosphine in chemical beam epitaxy [25] and MOVPE [94], also via the VLS mechanism. InP can also be synthesized in high purity in MOVPE using PH_3 and TMIn as chemical precursors, which was used to grow periodic InP nanowire arrays [95]. In InP nanowires the hexagonal wurtzite crystal structure has been observed with a direct band gap of 1.4 eV at room temperature [81, 96]. Compared to other III–V semiconductors, excluding nitrides, InP nanowires have an exceptionally low surface recombination velocity [97, 98].

In contrast to Si nanowire growth, the VLS mechanism of III–V semiconductors cannot easily be explained by a binary phased diagram, as three elements are involved. Therefore, the ternary phase diagram A_{III}–B_V–Au is necessary to predict the thermodynamically stable phases. Unfortunately, the In–P–Au ternary phase diagram is not available, but the three binary phase diagrams can be considered.

The In–P phase diagram (Figure 2.10a) is the simplest. Besides In and P, only one stoichiometric phase exists—InP. The Au–P phase diagram (Figure 2.10b) looks unusual because at the melting temperature of Au, P is already gaseous. While up to 13.5 % P are soluble in liquid Au, the necessary temperature of 935 °C is far above typical growth temperatures of InP, at which the solubility of P in Au can be neglected. Note that the Au–P phase diagram is based on white phosphorus and the In–P phase diagram is based on red phosphorus, which explains the different melting temperatures of P.

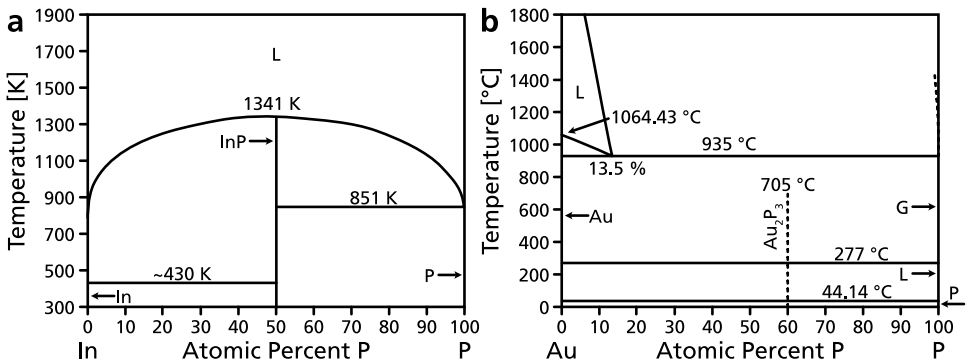

Figure 2.10: (a) In–P phase diagram. Adapted with permission from [99]. © 1997 Elsevier Ltd. (b) Au–P phase diagram. Adapted with permission from [100] © 1984 Springer.

The Au–In phase diagram (Figure 2.11) shows several phases and the two intermetallic compounds AuIn and $AuIn_2$. Apart from the melting point of In, the lowest eutectic melting point is 454.3 °C. However, it is known that the seed particle during Au-seeded InP nanowire growth is liquid at 420 °C. The following reasons might explain a reduced melting point: (i) The melting temperature can be slightly reduced for small nanoparticles; however, this effect is negligible for nanoparticles with diameters above ~100 nm. (ii) The phase diagrams are measured at atmospheric pressure, while nanowire growth is often performed at reduced pressures (typically 100 mbar for MOVPE). Nevertheless, as the molar volume during melting does not significantly change—in contrast to evaporation or sublimation—the dependance of the melting temperature on the pressure is normally neglected. (iii) Even though P is neither significantly soluble in In, nor in Au, its presence might affect the melting temperature of the Au–In alloy.

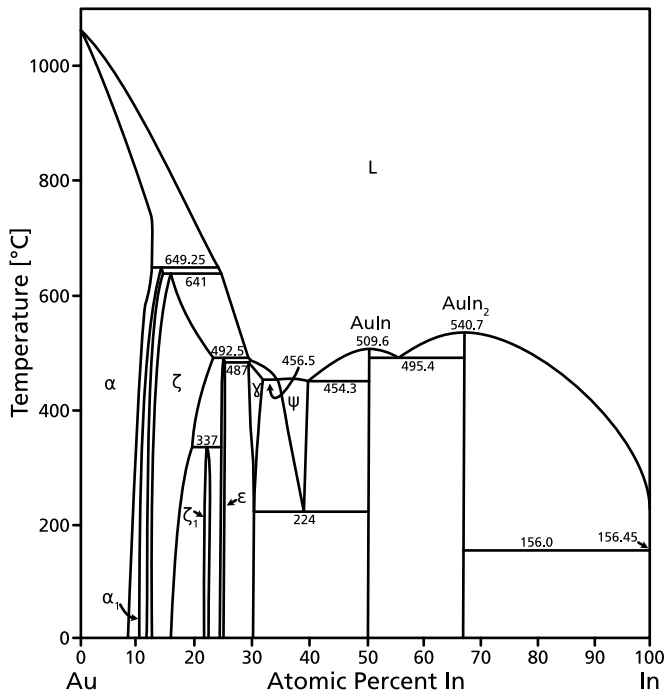

Figure 2.11: Au–In phase diagram. Adapted with permission from [101]. © 2017 Royal Society.

Another important note is, that Au is neither soluble in In nor P. While the ternary Au–In–P, or at least a pseudo-binary Au–InP, phase diagram would be necessary to determine the solubility of Au in InP, it can be assumed that a negligible amount of Au is incorporated in the growing InP crystal.

2.3.2 Indium Arsenide Phosphide

Indium arsenide phosphide ($InAs_xP_{1-x}$) is a solid solution of InP and InAs. The band gap can be adjusted by tuning the composition from pure InP ($x = 0$, $E_g = 1.34$ eV) to pure InAs ($x = 1$, $E_g = 0.35$ eV). Therefore, $InAs_xP_{1-x}$ is an interesting material for infrared detectors and light emitting diodes, or—as used in Paper V—as a bottom-cell in a triple-junction. The growth of $InAs_xP_{1-x}$ nanowires via the VLS mechanism is very similar to the growth of InP nanowires, as neither P nor As are soluble in the seed particle and the whole compositional range is accessible via the VLS mechanism [102, 103]. In addition to PH_3, AsH_3 is supplied via the gas phase.

2.3.3 Gallium Indium Phosphide

Gallium Indium Phosphide ($Ga_xIn_{1-x}P$)—a solid solution of InP and GaP—is another ternary III–V semiconductor. As mentioned before, GaP is one of the few III–V semiconductors that has an indirect band gap of 2.24 eV in the zincblende crystal structure. Therefore, the direct band gap of $Ga_xIn_{1-x}P$ is limited to a range of $0 \leq x \leq 0.68$ [104], corresponding to 1.34-1.97 eV, although in nanowires, wurtzite GaP with a direct band gap of 2.1 eV has been synthesized [105]. The most studied and used composition is $Ga_{0.5}In_{0.5}P$, as it is lattice-matched to GaAs and Ge and is used as a top-cell in planar multi-junction solar cells.

Even though the compositional range of $Ga_xIn_{1-x}P$ is limited regarding direct band gap applications, the whole range is accessible via the VLS mechanism. This is astonishing, as the InP–GaP pseudo binary phase diagram has a miscibility gap at typical growth temperatures [106]. Other than $IIIV_xV_{1-x}$ ternary solid solutions, in $III_xIII_{1-x}V$ ternary solid solutions, the composition of the seed particle is strongly affected by the additional group III precursor. Therefore, additionally to the Au–In phase diagram the Au–Ga phase diagram is relevant. For a better understanding, the ternary Au–In–Ga phase diagram needs to be considered, which has been thermodynamically modeled [107].

2.3.4 Doping of Nanowires

In addition to band gap engineering, doping is needed for many applications [108, 109]. By doping a semiconductor, impurities are introduced to the material that increase the amount of charge carriers. Impurities with more valence electrons than the atoms they replace in the crystal lattice increase the free electron concentration—this is referred to as n-type doping. On the other hand, if atoms of the crystal lattice are replaced with impurities that have fewer valence electrons, the free hole concentration is increased, which is referred to as p-type doping. According to the law of mass action, the product of the electron concentration and the hole concentration is constant. Thus, the chemical potential of the electrons, the Fermi level E_F, is higher in an n-type

semiconductor and lower in a p-type semiconductor. The probability of finding charge carriers in the valence or conduction band is given by the Fermi-Dirac distribution:

$$f(E)=\frac{1}{e^{(E-E_F)/k_B T}+1} \tag{2.4}$$

Where $f(E)$ is the probability to occupy a state at the energy E, k_B the Boltzmann constant and T the temperature. At E_F the probability to occupy a state is always 0.5, even if there are no available states at that energy.

Figure 2.12 shows the band structures of a p-type, an intrinsic, and an n-type semiconductor. Due to the different doping levels, the position of E_F is changed. As a result, a p-type semiconductor has more holes in the valence band and an n-type semiconductor more electrons in the conduction band than an intrinsic semiconductor. In a first approximation, the band gap E_g does not change.

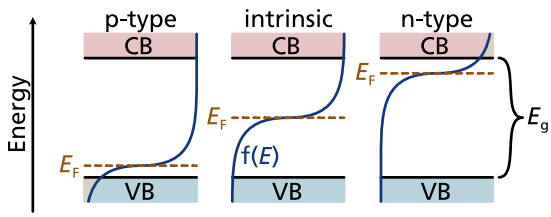

Figure 2.12: Band structures of (a) a p-type semiconductor, (b) an intrinsic semiconductor, and (c) an n-type semiconductor.

For III–V semiconductors, elements from group II or divalent transition metals can be used as p-dopants, while elements from group VI or tetravalent metals can be used as n-dopants. As group IV lies between group III and V, its elements are amphoteric dopants. That means that they can be incorporated in either the cation or the anion lattice and act as n- or p-dopant, respectively. While Si typically is an n-dopant in planar GaAs layers, it is often a p-dopant in VLS grown nanowires [110]. Whether Si is incorporated in the anion or cation lattice can be controlled by the V/III ratio during nanowire synthesis [111].

Aside from more exotic approaches to dope nanowires such as using a seed particle that is partly incorporated into the nanowire, a more flexible strategy is to add similar precursors as for the nanowire material, but in lower concentration, into the reaction chamber. For III–V semiconductor nanowires the chemical precursors diethylzinc (DEZn) [78, 112-114], dimethylzinc (DMZn) [115, 116], and bis(η^5-cyclopentadienyl)magnesium (magnesocene, Cp_2Mg) [117] can be used as p-dopants,

while tetraethyltin (TESn) [115, 118, 119], hydrogen sulfide (H_2S) [114, 120], and di-*tert*-butyl selenide (DTBSe) [118] can be used as n-dopants.

Even nominally intrinsic semiconductors are normally either n- or p-type due to intrinsic defects that can act as donors or acceptors depending on the material. Nominally intrinsic InP tends to be n-type [121], due to, *e.g.*, P-vacancies [122]. For solar cells, p–i–n junctions [123] are used to increase the short circuit current. In order to achieve such an intrinsic segment in an axial segment of an InP nanowire, the intrinsic doping needs to be compensated [124].

Doping incorporation in nanowires can differ from the doping incorporation in thin films, especially if a seed particle is used. First of all, the dopants can be incorporated in the nanowire crystal both from the top growth front as well as the sidewalls. Even if radial growth is suppressed, *e.g.*, by *in situ* etching [125], dopants might adsorb at the sidewall. Some dopants have high enough diffusion constants to allow solid diffusion towards the edge, after having been incorporated in the crystal. Typically, it is desired to incorporate dopants at the growth front beneath the seed particle. If the solubility of the dopant in the seed particle is high, it can result in a reservoir effect, *i.e.*, after switching off the dopant precursor flux, the seed particle acts as a reservoir that continues to supply dopant. This effect makes the creation of sharp doping profiles more difficult.

Another challenge regarding dopant incorporation is not unique to nanowires but applies to thin films as well. It is not sufficient to incorporate the dopants anywhere in the crystal. Normally, they have to be in the correct lattice positions, substitutional to either the group III or V lattice site, and not at interstitial positions. Furthermore, even if the dopant is incorporated at a substitutional lattice site, it needs to be ionized to contribute to the charge carrier concentration of the semiconductor.

Conventional Hall-measurements, that are typically used to measure charge carrier concentrations, are difficult to apply to the nanowire geometry. Therefore, determining the charge carrier concentration in nanowires is not trivial, especially for low doping concentrations. However, the progress in nanofabrication in recent years made it possible to measure the Hall effect on single nanowires [126, 127].

Instead of measuring the charge carrier concentration it is also possible to measure the concentration of dopant atoms, even though not all of them are necessarily incorporated in the correct crystal lattice sites and ionized. Especially if spatial resolution is of importance, the detection of the dopant atoms can be challenging as well and non-standard techniques such as X-ray fluorescence of a focused X-ray beam from, *e.g.*, a synchrotron source have to be used [128].

2.3.5 *In Situ* Etching

For many applications, especially for axial heterostructures, it is important to avoid radial growth during nanowire synthesis. While the growth conditions for VLS grown nanowires can be optimized for preferential nucleation at the triple phase boundary of the seed particle, there is always a small chance for parasitic crystal growth at the nanowire sidewalls. In order to prevent such radial crystal growth, hydrogen chloride (HCl) [125], or the stronger acid hydrogen bromide (HBr) [129], can be introduced in the reaction chamber together with the other precursors, as an *in situ* etchant. In addition to preventing radial growth, *in situ* etching enhances the parameter space for successful nanowire growth without kinking, and improves the charge carrier dynamics [130].

2.4 Chemical Analysis

Once the nanowires are synthesized, chemical analysis is necessary to verify that the intended material was obtained. In the case of III–V semiconductors, this is especially important for the chemical composition of ternary or higher solid solutions.

2.4.1 X-Ray Diffraction

In an X-ray diffractogram, Bragg's law (2.5) is used to obtain the atomic spacing d of crystallographic planes. A prerequisite for the measurement is therefore that the sample is crystalline. The wavelength λ should be in the order of the atomic spacings, and often the Cu K_α line (0.15406 nm) is used in experiments. In a simplified picture, constructive interference occurs when the phase difference $2d{\cdot}\sin(\theta)$, between two waves with incident and emergent angles of θ, is an integer n multiple of λ (Figure 2.13). In an experiment, goniometers are used to rotate the angle θ between the X-ray source and the sample, and the angle 2θ between the X-ray source and the detector.

$$n\lambda = 2d\sin(\theta) \tag{2.5}$$

Using the atomic spacing of a given crystallographic plane, the lattice constant a of the material can be obtained. According to Vegard's law, the composition of a solid solution of two compounds that have the same crystal structure can be obtained using a linear interpolation of the lattice constants.

$$a_{A_xB_{1-x}C} = x\cdot a_{AC} + (1-x)\cdot a_{BC} \tag{2.6}$$

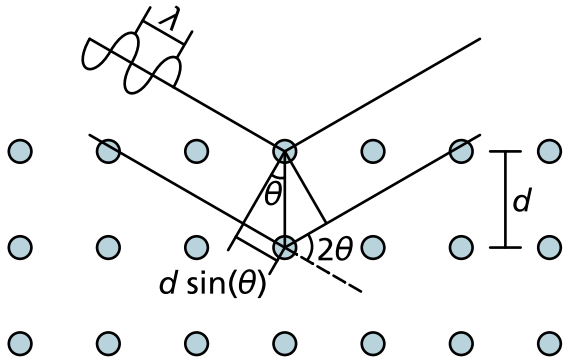

Figure 2.13: Schematic explanation of Bragg's law. Two waves with wavelength λ are scattered at crystallographic planes with lattice spacing d. Constructive interference occurs when the angle between the X-ray source and the detector is twice the incidence angle θ, and when the induced phase difference $2d\sin(\theta)$ is an integer multiple of λ.

2.4.2 Photoluminescence

In a photoluminescence (PL) measurement, a monochromatic laser is used to excite the electrons of a semiconductor from the valence band to the conduction band. After thermalization of the charge carriers, the charge carriers recombine and emit photons corresponding to the band gap of the semiconductor.

Although the band gap E_g of ternary solid solutions of III–V semiconductors is continuous, it is not a linear function in contrast to the lattice constant. Instead, a so-called bowing parameter b is introduced to account for the non-linear dependence.

$$E_{g,A_xB_{1-x}C} = x \cdot E_{g,AC} + (1-x) \cdot E_{g,BC} - b \cdot x(1-x) \tag{2.7}$$

Even though the band gap can thus be used to deduce the chemical composition of a ternary solid solution, the method depends on tabulated bowing parameters and band gaps of bulk materials that are not necessarily representative for nanomaterials. However, for many applications the band gap is more important than the actual chemical composition.

2.4.3 Electron Microscopy

The diameter of nanowires is smaller than the wavelength of visible light. Thus, due to the Abbe diffraction limit, nanowires cannot be properly resolved in conventional optical microscopy. Instead, electron microscopy is often used to image nanostructures.

In a scanning electron microscope (SEM), a focused electron beam is scanned across a conductive sample. Figure 2.14 shows the possible interactions of the electron beam with the sample that can be used for imaging and chemical analysis.

Energy dispersive X-ray spectroscopy (EDXS) can be measured both in an SEM and with scanning transmission electron microscopy (STEM). The electron beam can excite electrons from inner shells of the investigated material. Subsequently, an electron from a higher shell may relax to the lower available state and a characteristic X-ray photon is emitted. Even though the electron beam can be focused to a spot size of ~1 nm, EDXS in a SEM suffers from low spatial resolution because X-rays generated in the whole interaction volume—which can be in the order of ~1 µm depending on the accelerating voltage and sample—are measured. In STEM, only thin samples can be investigated and here high spatial resolutions of few nm can be achieved.

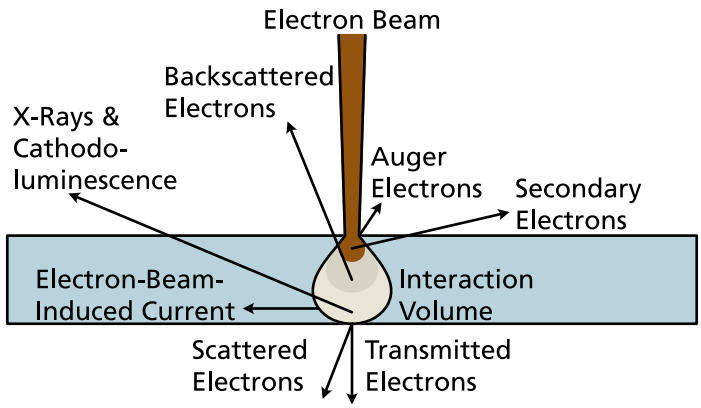

Figure 2.14: Possible interactions of a focused electron beam with a sample. Auger electrons have the lowest energy and are therefore the most surface sensitive, followed by secondary electrons and backscattered electrons. Cathodoluminescence, X-rays, and electron-beam-induced current have the lowest surface sensitivity.

2.5 Nanopatterning

In order to synthesize Au-seeded nanowires via the VLS mechanism, Au nanoparticles need to be deposited on a growth substrate. This has been achieved by drop casting of colloidal Au nanoparticles [131] and aerosols [25]. Depending on the wetting properties, on some growth substrates it is sufficient to deposit a thin Au film, which will self-assemble to droplets at elevated temperatures [23, 24]. However, these methods result in a random deposition of Au seeds, and it can be of advantage to synthesize nanowires in ordered, periodic arrays. To achieve that, lithography is necessary.

2.5.1 Nanoimprint Lithography

In nanoimprint lithography (NIL), a nanopatterned stamp is used to imprint a photoresist on a wafer to transfer the pattern onto the wafer [132], as depicted in Figure 2.15. In order to fabricate a periodic pattern of Au discs on a growth substrate, a wafer is covered by two layers of resist: (i) lift-off resist, and (ii) photoresist. Starting from a Ni master stamp, an intermediate polymer stamp (IPS) is formed. Using the IPS has the advantage to prevent physical damage of both the Ni master stamp as well as the growth substrate, to reduce the defect size caused by contaminations, and to enable the use of UV light to harden the negative photoresist. The IPS is then used to imprint the photoresist on the growth substrate (Figure 2.15a) by applying pressure and exposing the photoresist to UV light. In order to transfer the pattern to the substrate, first, residual photoresist (Figure 2.15b) needs to be etched, *e.g.*, using reactive ion etching (Figure 2.15c). Then, the underlying lift-off resist needs to be developed (Figure 2.15d) to release the surface of the growth substrate and to create an undercut. Afterwards, Au is evaporated onto the substrate (Figure 2.15e). Finally, excess lift-off resist that is covered by Au can be removed to result in cylindrical Au discs on the growth substrate (Figure 2.15f).

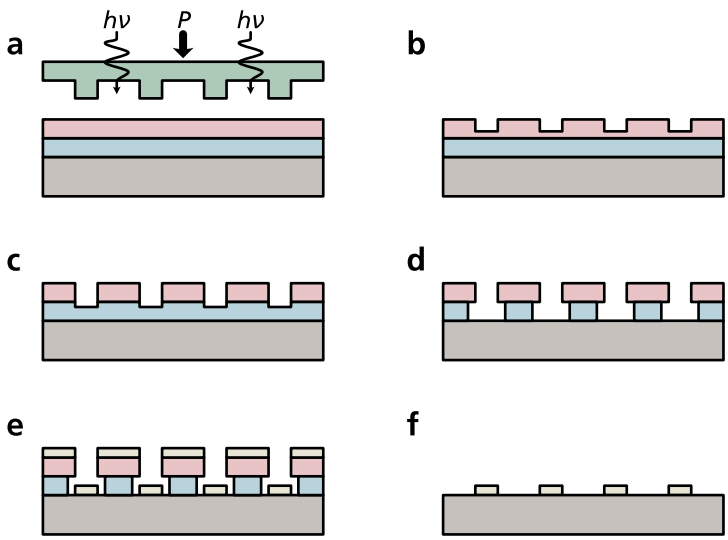

Figure 2.15: Schematic of the steps involved in NIL. (a) Two layers of resist are deposited on a wafer. The pattern of a stamp is transferred to the top resist. (b) After the imprint, a residual layer remains in the top resist. (c) Reactive ion etching is used to etch the residual layer of the top resist. (d) Development of the bottom resist reveals the surface of the wafer and creates the undercut necessary for the subsequent lift-off process. (e) Metal evaporation. (f) Using remover, the excess resist and metal are removed in a lift-off process.

2.5.2 Displacement Talbot Lithography

Displacement Talbot lithography (DTL) is an optical lithography technique that can achieve sub 100 nm resolution [133-135]. A periodic phase-shift mask is exposed to a deep UV laser, which results in a 3D diffraction image below the phase-shift mask. Similar to NIL, the wafers are coated with a double resist layer. During exposure (Figure 2.16a), the photoresist-covered wafer is vertically moved through the diffraction image of the mask, which results in a homogenous exposure of the photoresist. Subsequently, the photoresist is developed (Figure 2.16b). In contrast to NIL, no etching step to remove residual photoresist is necessary and the underlying lift-off resist can be developed at the same time. After Au evaporation (Figure 2.16c) and lift-off (Figure 2.16d), a periodic array of Au discs is obtained. In comparison with NIL, DTL reduces the number of processing steps and avoids mechanical contact with the resist layers, which reduces the number of defects. Furthermore, the feature size can be adjusted in DTL by adjusting the exposure dose. This was utilized in Paper I to synthesize nanowire arrays with different diameters.

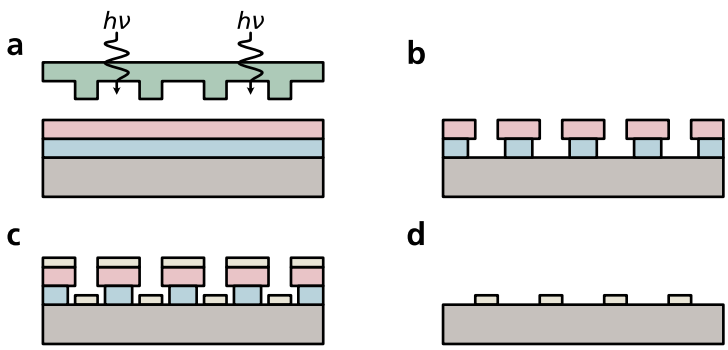

Figure 2.16: a) Schematic of the steps involved in DTL. (a) Two layers of resist are deposited on a wafer. A phase-shift mask is used to transfer a periodic pattern to the wafer under exposure to a deep UV laser. During exposure the wafer is vertically moved through the Talbot period. (b) After the exposure, both resists are developed simultaneously. (c) Metal evaporation. (d) Using remover, the excess resist and metal are removed in a lift-off process.

2.5.3 Pattern Fidelity

The pattern fidelity of a nanowire array will foremost depend on lithography. Defects in the NIL stamp or DTL mask will be transferred to the growth substrate and subsequently cause a defect in the nanowire array. Additionally, precautions have to be taken regarding the nanowire synthesis. Epi-ready wafers have a thin, native oxide that needs to be removed in an annealing step prior to nanowire growth [136-138]. Even though the temperature during the annealing is far below the melting point of Au and

no group III flux is provided via the gas phase, the group III elements from the growth substrate can be dissolved in the Au seeds [139, 140]. This results in a reduction of the melting-point and liquid droplets are formed that may diffuse on the surface. This can cause an alteration of the periodic array, and in the worst case droplets merge together, completely destroying the periodicity [141].

In order to obtain the pattern fidelity, two main approaches are used. First, an inert growth mask can be used to prevent the migration of the seed droplets during the annealing step. In practice, a thin layer of Si_3N_4 or SiO_2 is deposited on the growth substrate prior to lithography, and holes are etched into the growth mask before evaporating Au. Although this method can lead to defect-free nanowire arrays, the growth mask alters the diffusion length of the precursors and might affect the doping at the interface between the nanowires and the growth substrate. Alternatively, in the case of InP substrates, a pre-annealing nucleation step has been utilized to maintain the pattern fidelity during annealing [141]. In this approach, prior to the annealing step, TMIn was supplied at a low temperature. From cross-sectional SEM images no direct effect on the seed particles, which were still solid, was observed. However, during the annealing step the Au seeds consume In from the substrate, forming indentations. The pre-annealed Au seeds are presumably enriched with In—according to Figure 2.11 about 9 % In are soluble in the solid α phase. Therefore, during the annealing step, the composition at which the particles melt is reached faster and the droplets are fixated within the indentations before the droplets can coalesce [141]. Such a pre-annealing nucleation step has been utilized in Papers I-V.

3 Surface Passivation

Due to their small size, nanostructures—including nanowires—have a much higher surface-to-volume ratio than bulk materials. Surfaces are special because the periodicity of a crystal is abruptly interrupted, leading to so-called dangling bonds. In order to minimize the resulting surface energies, semiconductor surfaces can undergo surface reconstruction during synthesis.

Exposed to ambience, those dangling bonds are normally not very stable and can react with oxygen or water to form an oxide or hydroxide layer, respectively. Depending on the material, the resulting layers can protect the underlying bulk substance and are sometimes even purposefully provoked as in thermal silicon oxide or anodized aluminium oxide, or slowly disintegrate the material like the rusting of iron.

For III–V semiconductors, the native oxide lies in-between those two extremes. Normally, exposure to air will not destroy the bulk material, but surface traps can lead to non-radiative recombination centers [97] and therefore have a detrimental effect on optoelectronic properties. Consequently, it is of great interest, especially for nanostructures, to passivate the surface of III–V semiconductors.

3.1 Epitaxial Passivation

The most natural way to passivate nanowires is to epitaxially grow a shell, typically with higher band gap [29, 142, 143]. In this way, the core crystal is never exposed to ambience and the pristine surface of the as-grown nanowire can be passivated before a native oxide forms. In order to have a passivating effect, the epitaxial shell has to fulfil some requirements. Ideally, the shell material should be lattice matched to the core material. Otherwise, the resulting strain might have a negative effect on the nanowire, compromising the passivating effect. On the other hand, inducing strain on purpose can be used for band gap engineering [144] or to increase mobility of charge carriers [145]. It has to be kept in mind that even if a lattice matched shell is deposited in the growth chamber, it might not be lattice matched anymore at room temperature due to different thermal expansion coefficients of the materials of the nanowire core and shell but for III–V semiconductors the difference in thermal expansion coefficients is small. Secondly, for many applications, a shell with a higher band gap than the core

material is desired to prevent charge carriers to diffuse into the shell material. The shell should also be highly electrically resistive to prevent possible radial short circuits of an axial nanowire device. Another challenge that the epitaxial passivation of nanowires poses is that the passivation layer can cause modulation doping [29, 146-148] and form an undesired radial p–n junction [149].

3.2 Wet Chemical Modifications

Often, wet chemical treatments are used to satisfy the dangling bonds at the surface. Generally, the idea is that the native oxide is etched away, and the surface terminated by another functional group at the same time. For silicon, an HF dip leads to a hydrogen terminated surface [150]. The surface of III–V semiconductors can be passivated with chalcogenides [151]. For InP, wet chemical treatments based on sulfur [152] and phosphor [153] groups have been reported.

Even though wet chemical treatment of semiconductor surfaces can have a positive effect on their optoelectronic properties, these effects are often of limited duration [154] and after some time the chemically more stable native oxide will form again [155].

3.3 Deposition of Dielectrics

As an alternative, or complement [156], to wet chemical treatments, dielectrics can be deposited on the semiconductor surface, typically by CVD methods. Especially atomic-layer-deposition (ALD) has proven useful [157], as this technique fulfils the requirement of being able to conformally deposit layers of a controlled thickness. Another method that has been used to deposit dielectric layers on nanowire surfaces is plasma enhanced CVD [158].

These dielectric layers have the advantage of being thermally stable, and their passivation performance will not change over time. For InP nanowires, SiO_x [124] and PO_x/Al_2O_3 [159] have been used as passivation layers. However, many dielectrics deposited that way have a negative effect on the optoelectronic properties of the nanowire cores [160, 161]. On the one hand, the deposited layers can introduce charge carrier traps at the core-shell interface and on the other hand, fixed charges in the shell can have a field-effect on the nanowire core that changes its electrostatic potential [162]. It is of great importance to measure how well dielectrics passivate or deteriorate the nanowire and this issue has been addressed in Paper II on SiO_x and PO_x/Al_2O_3 passivated InP nanowires.

3.3.1 Atomic Layer Deposition

Atomic layer deposition (ALD) is a subcategory of CVD. During deposition the sample is cyclically exposed to chemical precursors. Each cycle results in one atomic layer. In addition to the high precision of the layer thickness, even high-aspect samples such as nanowires can be covered conformally using ALD. Each cycle consists of several steps, and often two different precursors are used alternatingly (Figure 3.1). In a typical ALD process, a precursor is chemisorbed at the surface and forms a monolayer. Then, after a purging step, a second precursor reacts with the monolayer to form the deposit and the cycle can be repeated.

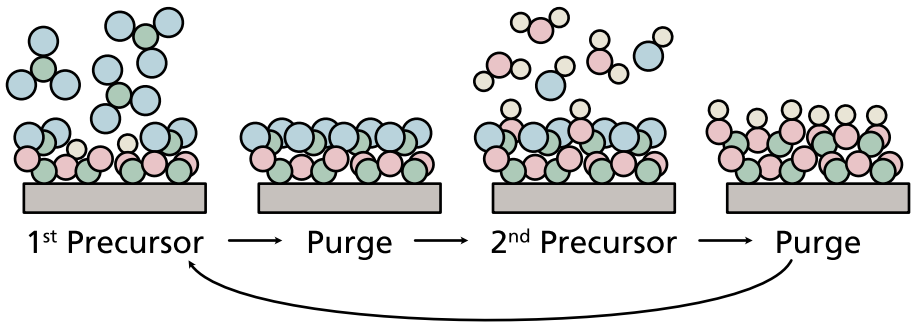

Figure 3.1: Schematic ALD cycle.

3.4 Evaluation of Surface Passivation

One way to quantify the surface passivation is to measure the PL of a semiconductor. Traditional PL can resolve the wavelength (or energy) of the emitted light and measure the intensity. Often, PL intensities are compared to estimate the passivation of semiconductors. A more sophisticated technique is time-resolved PL (TRPL). Instead of, or additionally to, resolving the wavelength of the emitted light, the time t at which the photon is emitted after excitation is measured. By varying the laser power, statements about surface traps can be made, which are saturated at higher illumination intensities [163]. The charge carrier lifetime can be obtained by fitting the PL decay. The lifetime of the excited states is relevant for photovoltaics. The assumption is that a longer lifetime leads to a higher probability to separate charge carriers in a p–n junction, thus contributing to the photocurrent. Other time-resolved techniques to evaluate surface passivation are transient absorption spectroscopy [164] and time-resolved terahertz spectroscopy [97, 98]. Furthermore, electron-beam-induced current (see Chapter 4.2.3) has been used to measure the minority carrier diffusion lengths [154].

4 Nanowire Solar Cells

III–V Nanowires are excellent light absorbers. Due to their geometry, nanowires absorb light from a larger area than their own cross-section. Consequently, using nanowires, only a fraction of the material is needed to absorb the same number of photons as a continuous thin film, thereby saving up to 90 % of the III–V semiconductor. Therefore, nanowires are an interesting material for solar cells because the high cost of III–V semiconductors limits the terrestrial use of world record solar cells. Nanowire solar cells are actively researched, and several reviews exist, summarizing recent developments [12-15, 165, 166]. The highest efficiencies so far have been reached in InP nanowire solar cells [124, 167, 168], accomplishing 17.8 % in a top-down processed device [169]. To be used as a solar cell, it is not sufficient to only absorb light—the generated charge carriers have to be separated to generate a photocurrent. While this separation can be achieved by utilizing charge-carrier-selective contacts [170, 171], typically a p–n junction is formed by doping.

4.1 p–n Junction

Doping of nanowires has already been discussed, but just a p- or n-doped nanowire is not enough to make a solar cell. By consecutively combining both, a p–n junction is formed. In equilibrium, the fermi level of both parts is at the same energy, creating an offset in the valence and conduction bands of the semiconductor (Figure 4.1a). If a voltage V_R is applied in reverse direction, *i.e.*, a negative potential is applied to the p-type segment (Figure 4.1b), the depletion width W gets even wider and no current flows, until the breakdown voltage is reached. If a voltage V_F is applied in forward direction, *i.e.*, a negative potential is applied to the n-type segment (Figure 4.1c), W becomes narrower and current can flow through the diode. The potential difference between the p-segment and n-segment is proportional to the sum of the built-in voltage V_{bi} and the external applied voltage.

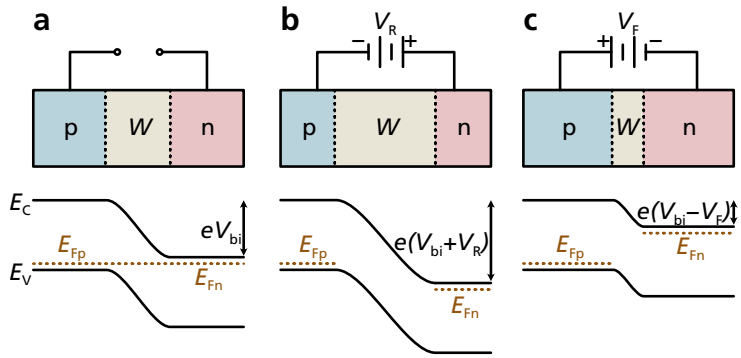

Figure 4.1: p–n junction of a semiconductor. (a) Without an external voltage, the Fermi level of the n-segment and the p-segment are in equilibrium. (b) When a voltage is applied in reverse direction, the depletion width gets wider, and no current can flow through the diode. (c) When a voltage is applied in forward direction, the depletion width gets narrower and current can flow through the diode. Adapted with permission from [172].

4.1.1 Axial vs Radial Geometry

The nanowire geometry enables an additional design of p–n junctions. If a thin film is etched into nanowires, the p–n junction is located along the nanowire axis. Via bottom-up synthesis, it is also possible to form a radial p–n junction. It is a matter of ongoing research whether radial or axial p–n junctions lead to better nanowire solar cells and both designs have their merits [173].

Radial p–n junctions have the advantage of separating the direction of the incoming light and the separation of charge carriers [174, 175]. In thin films, a compromise has to be found between a depletion region that is thick enough to sufficiently absorb light, but thin enough to allow the separation of charge carriers. In a radial p–n junction, these two parameters can be optimized independently by the length and diameter of the nanowires. Furthermore, the active region of the radial p–n junction is not affected by the high surface-to-volume ratio of nanowires. However, radial designs are limited to similar lattice matching requirements as thin films. Furthermore, the low V_{OC} observed in the radial geometry indicates that the extension of the p–n junction all across the nanowire leads to a shunt.

While the axial p–n junction design in nanowires has been underestimated in early studies, all record efficiency devices are based on this design [142, 167, 169]. Nanowire solar cells based on InP are not limited by the high surface-to-volume ratio due to the low surface recombination velocity of InP [97, 98]. Nanowire solar cells based on GaAs on the other hand, were epitaxially passivated by an AlGaAs shell [142], although the presence of an epitaxial shell might have caused a radial junction [149]. The obvious

advantage of an axial p–n junction architecture is that lattice mismatched materials can be combined to form sub-cells with different band gaps in multi-junction technology.

To combine the advantages of both approaches, a design that axially combines radial p–n junctions with different bandgaps has been suggested [176]. In theory, such an architecture sounds very intriguing, although an experimental realization seems to be extremely challenging.

4.2 Single Nanowire Measurements

In order to measure current–voltage (I–V) characteristics of nanowires, processing is typically necessary to provide electric contacts to the nanowire. Not only is the processing time-consuming, but it can also be challenging to get an ohmic contact. This depends on the material and on the doping. For example, it is demanding to achieve ohmic contacts to p-doped InP [177]. Furthermore, horizontally processed nanowires have to be removed from the growth substrate before contacting. Therefore, the fabricated devices might not be representative for vertically processed samples such as nanowires solar cells.

4.2.1 Nanoprobing

One possible alternative is to contact nanowires with a conductive probe. Conductive scanning probe microscopy (SPM) tips have been used to contact single, epitaxial nanowires [34, 178]. Single nanowire I–V characteristics can be measured using the substrate as a back contact and for VLS grown nanowires it is very convenient to get a good electrical contact to the metal seed particle. While the electrical measurements of single nanowires are certainly valuable, due to the high aspect ratio of nanowires, conventional scanning probe microscopy can only image the top of epitaxially standing nanowires. In a more sophisticated setup, SPM was performed inside a SEM [179]. This enables to characterize single nanowires with the conductive SPM tip and simultaneously image the nanowires using SEM. A similar, though instrumentally simpler, approach is to use piezo-controlled nanoprobes [180, 181] that can be controlled inside a SEM. Figure 4.2 shows a photograph of the Kleindiek prober shuttle that was used to analyze single nanowires in Papers I-V. After contacting the nanowire, a source-meter can be used to measure I–V characteristics.

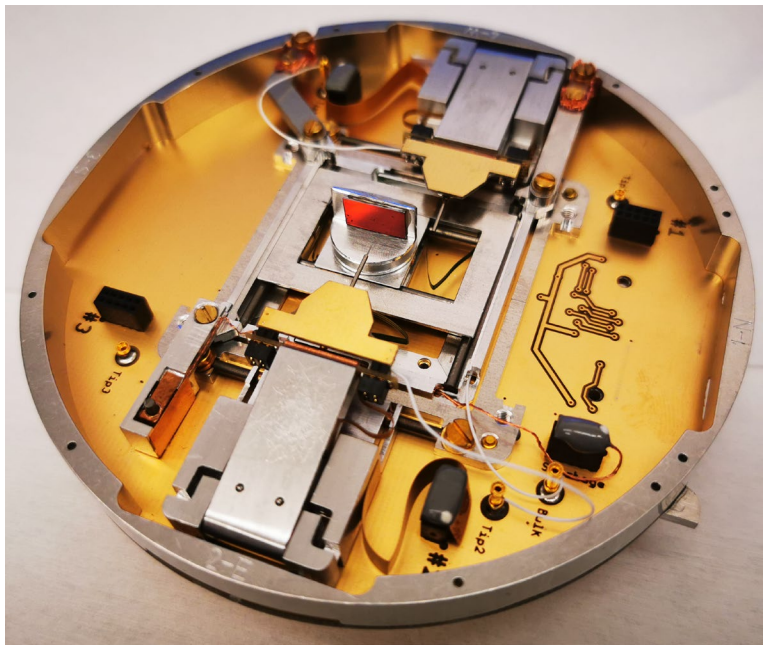

Figure 4.2: Kleindiek prober shuttle used to electrically contact single nanowires inside an SEM. Two independent probes and the substage of the sample can be moved in three dimensions and used for electrical contacts.

4.2.2 Current–Voltage Characteristics

In the dark, the *I*–*V* characteristics of a solar cell can be described by the ideal diode equation (4.1) in which I_0 is the dark saturation current, e is the elementary charge of an electron, k_B is the Boltzmann constant, T is the temperature, and n is the ideality factor. The linear region of the curve in the semi logarithmic plot can be fitted to this equation to extract n and I_0. For nanowires, typically an n of about 2 is observed. An ideality factor of 2 indicates that recombination is limited by two charge carriers, which is the case within the depletion region and for trap-assisted Shockley-Read-Hall recombination. Surface recombination in nanowires can be described as a special case of Shockley-Read-Hall recombination [182].

$$I = I_0 \cdot \left(e^{\frac{eV}{nk_B T}} - 1 \right) \tag{4.1}$$

Under illumination, electron–hole pairs are generated in a solar cell. Without any contacts, the solar cell is in open-circuit voltage (V_{OC}) conditions which is the maximum voltage that can be reached with the solar cell. In contrast, a short circuit of the solar cell leads to the maximum current that can be extracted at 0 V, the short circuit current (I_{SC}). However, neither of these cases are useful for the operation of a solar cell, as both current and voltage are necessary to extract a power. The optimal working conditions of a solar cell are at the maximum power point (P_{MP}), where the power, the product of current and voltage, is the highest. From this value, the fill factor (FF) can be calculated:

$$FF = \frac{P_{MP}}{I_{SC} \cdot V_{OC}} \tag{4.2}$$

FF is therefore the ratio of the maximum possible power output to the theoretical maximum power possible. All these values can be measured for single nanowires as well. Obviously, single nanowires can be processed to working devices that are illuminated under light, but it is also possible to couple light into an SEM through an optical fiber to illuminate as-grown nanowires, as in Refs [179, 183]. In Paper III a similar setup is described, as schematically shown in Figure 4.3.

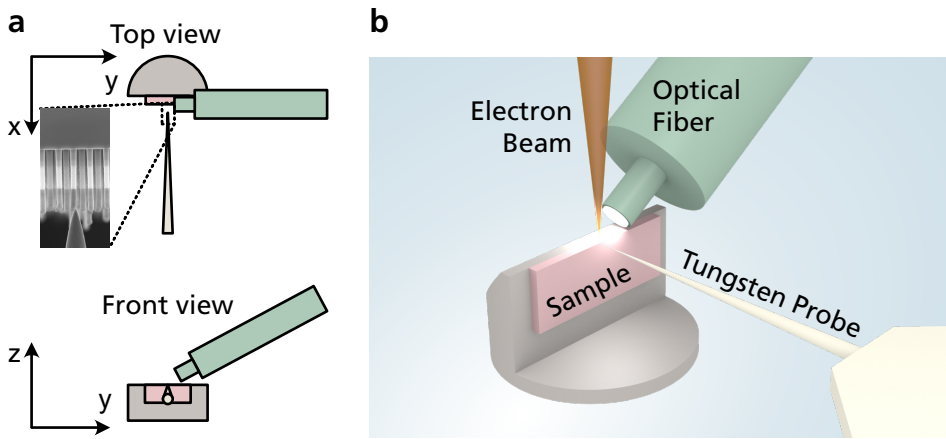

Figure 4.3: Schematic drawing of the combined multi-LED and nanoprobing setup. (a) Top and front view. Inset shows SEM image of a nanowire contacted by the piezo-controlled tungsten probe. Reproduced from Paper IV. (b) 3D rendering of the setup. Reproduced from Paper V.

Figure 4.4a shows a semi-logarithmic plot of the I–V characteristics of a single InP nanowire with a p–i–n junction, demonstrating the superposition of the I–V characteristics in the dark and under illumination. A fit of the diode equation to the dark I–V characteristics is used to extract I_0 and n. In Figure 4.4b the I–V characteristics

under light illumination are plotted on a linear scale to show I_{SC} and V_{OC}. The product of I and V yields the power P that has a maximum at P_{MP} that is used to extract FF.

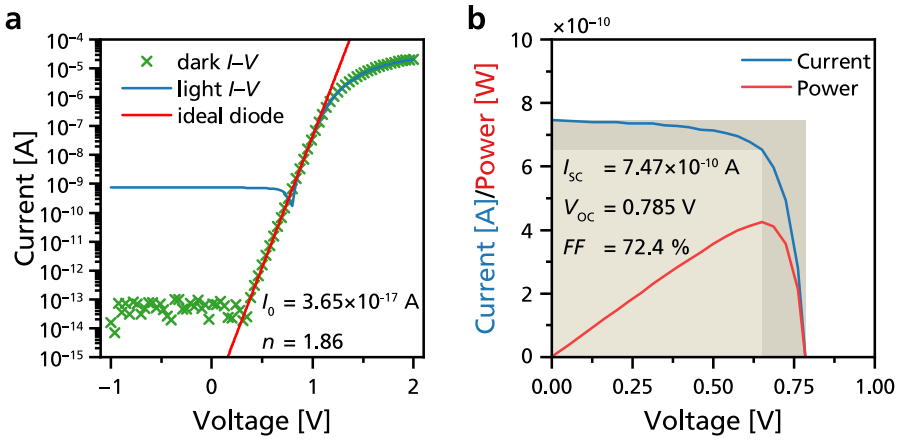

Figure 4.4: Single nanowire *I–V* characteristics. (a) Semi-logarithmic plot showing the superposition of dark and light *I–V* of a single photovoltaic nanowire and the fit of the ideal diode equation to extract n and I_0. (b) Linear plot showing the light *I–V* and power. I_{SC} and V_{OC} can be found at 0 V, and 0 A, respectively. *FF* corresponds to the ratio of the dark and light rectangle, which are defined by $I_{SC} \cdot V_{OC}$ and P_{MP}, respectively.

Typically, solar cells are not exposed to a constant light source. With varying intensity, the response of a solar cell is affected. A change in the intensity will change the number of excited charge carriers and thus the IV-characteristics. With increasing light intensity, both V_{OC} and I_{SC} increase according to equations (4.3) and (4.4), where χ is a factor describing the concentration of light. Furthermore, equation (4.4) shows that a low I_0 is essential to obtain a high V_{OC}. In Paper III, a systematic variation of the light intensity was conducted to extract n of single InP nanowires, and it matched the obtained ideality factor from the dark *I–V* measurements using equation (4.1).

$$I_{SC\chi} = \chi \cdot I_{SC} \tag{4.3}$$

$$V_{OC\chi} = \frac{n k_B T}{e} \ln\left(\frac{I_{SC\chi}}{I_0}\right) \tag{4.4}$$

4.2.3 Electron-Beam-Induced Current

Figure 4.5 describes electron-beam-induced current (EBIC), which is a very useful technique to investigate p–n junctions with the spatial resolution of an SEM [184,

185]. The investigated sample needs to be electrically contacted inside an SEM. Single nanowires can be investigated by EBIC either by defining metal contacts via lithography [62, 186-191], or by directly contacting the tip of a nanowire using piezo-controlled probes [124, 183, 192-199], as depicted in Figure 4.5a. Then, while scanning the electron-beam across the sample to generate an image, for every pixel that is exposed to the electron-beam of the SEM, the current through the sample is measured. The electron-beam excites electron–hole pairs in a similar fashion as light but while photons typically generate one electron–hole pair per incident particle, the high-energy electrons of an SEM (in the order of several keV) can generate thousands of electron–hole pairs simultaneously in the sample per incident particle. Therefore, if the generated charge carriers are separated, *e.g.*, by a gradient in the band structure of the sample (Figure 4.5b), an electron-beam-induced current will be measured (Figure 4.5c). Figure 4.5d shows an SEM image of an InP nanowire with a p–i–n junction (top) and the corresponding EBIC image (bottom) that is simultaneously obtained.

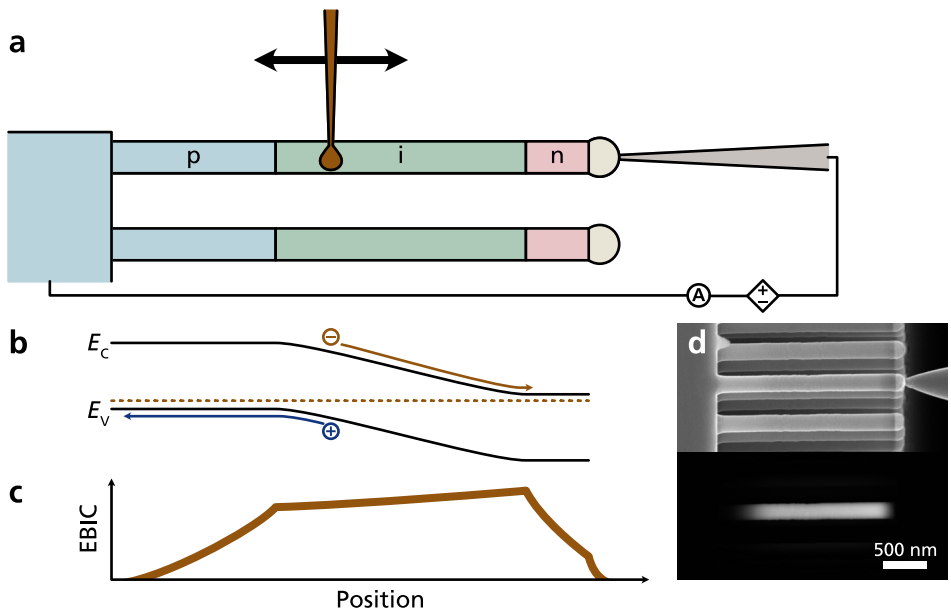

Figure 4.5: Schematic drawing of an EBIC measurement. (a) A single nanowire with a p–i–n junction is contacted by a piezo-controlled tungsten probe. During the measurement, the induced current is measured while a controlled voltage source can apply a bias—otherwise the circuit is grounded. A focused electron beam is scanned across the sample and generates electron–hole pairs within the excitation volume. (b) Due to the built-in electric field—or an applied voltage—the electron–hole pairs are separated. (c) The resulting EBIC can be plotted as a profile along the nanowire. (d) SEM (top) and EBIC (bottom) image of a photovoltaic InP nanowire.

EBIC can also be measured as I_{SC} if the sample is excited by the electron beam during an *I–V* measurement. Indeed, in Paper III it was shown that the axial EBIC profiles

along single photovoltaic nanowires correlate with I_{SC} of the nanowires under illumination of an LED. By using equation (4.3), the excitation level of the electron beam can be compared to a corresponding light concentration. However, this comparison is not trivial, as electrons are used as an excitation source instead of photons. Moreover, the incident angle is different for the cross-sectional EBIC measurements as compared to characterization of a processed solar cell.

EBIC can be used to measure the minority carrier diffusion length in nanowire p–n junctions [154]. The measured EBIC is proportional to the probability that a generated electron–hole pair contributes to the photocurrent of a solar cell. This probability can be modeled as a spatially resolved internal quantum efficiency (SIQE) [200, 201]. In Paper II the SIQE was modeled to analyze the influence of different charge carrier densities and surface recombination velocities and compared to measured EBIC profiles.

5 Multi-Junction Solar Cells

Single-junction solar cells have two main fundamental loss mechanisms that are both related to insufficient power conversion of the incoming solar spectrum. First, photons that have less energy than the band gap cannot be absorbed to generate photocurrent (below E_g loss). Second, charge carriers excited by photons that have more energy than the band gap thermalize, *i.e.*, their excess energy is lost to heat, before they can be extracted (thermalization loss). With other words, a material with a low band gap absorbs almost all photons and generates a high current, but the resulting voltage is very small. A material with a high band gap on the other hand, only absorbs high-energy photons which results in a high voltage, but the current is low as only few photons are absorbed. To optimize the power output, and with that the efficiency, a compromise needs to be found. The highest efficiency that can be achieved in a single-junction solar cell is known as Shockley-Queisser limit [202] and calculations show that the ideal band gap for a single-junction solar cell is 1.35 eV [203]. Other fundamental losses are the emission loss (because absorbers must also be emitters according to Kirchhoff's law), the Boltzmann loss (due to an increase in entropy during emission), and the Carnot loss (the ultimate efficiency limit for any heat engine) [204]. These fundamental losses and the maximum efficiency of a single-junction solar cell are shown in Figure 5.1a as a function of E_g.

The approach of multi-junction solar cells to increase the efficiency is to reduce the below E_g and thermalization losses by combining several materials with different band gaps to better match the solar spectrum. Similar to the Shockley-Queisser limit of a single-junction solar cell, there are ideal combinations of band gaps. Figure 5.1b shows the same fundamental losses and maximum efficiency as Figure 5.1a but dependent on the number of sub-cells for ideal band gap combinations.

Especially in two terminal devices it is crucial to match the currents of the sub-cells because all junctions are connected in series. That means that the current of the multi-junction solar cell is limited by the sub-cell generating the lowest current. If the band gaps of two consecutive sub-cells are too close, or in the worst case the same, the current of the bottom-cell will be limited as the relevant photons were already absorbed by the top-cell. Therefore, the band gaps have to be matched to the solar spectrum and need to descend from the top-cell to the bottom-cell. Figure 5.2a shows the reference global solar spectrum with an air mass of 1.5 (AM1.5g) [205]. In Figure 5.2b a schematic triple-junction solar cell is shown, representing the sample from Paper V.

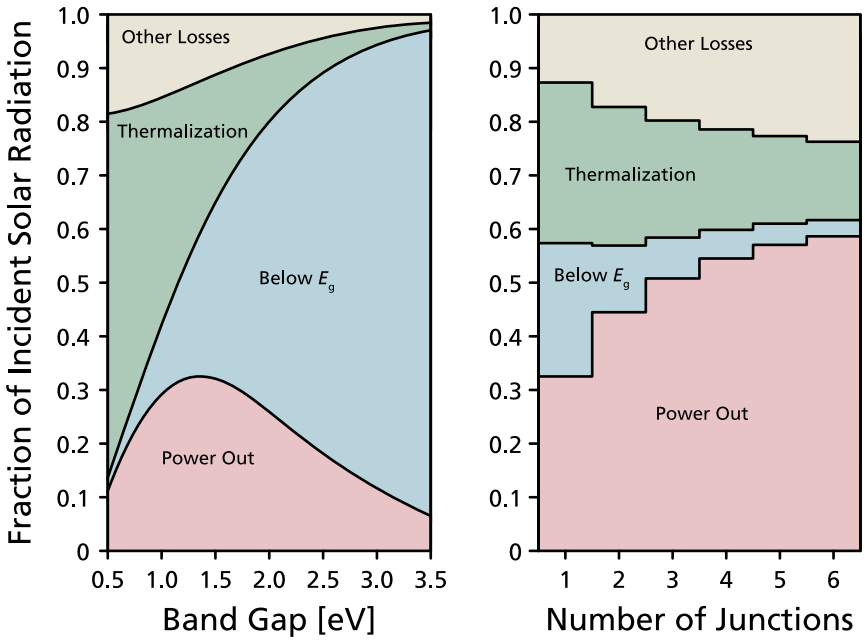

Figure 5.1: Fundamental losses, efficiency as function of bandgap and number of junctions. Adapted with permission from [204]. © 2010 John Wiley & Sons, Ltd.

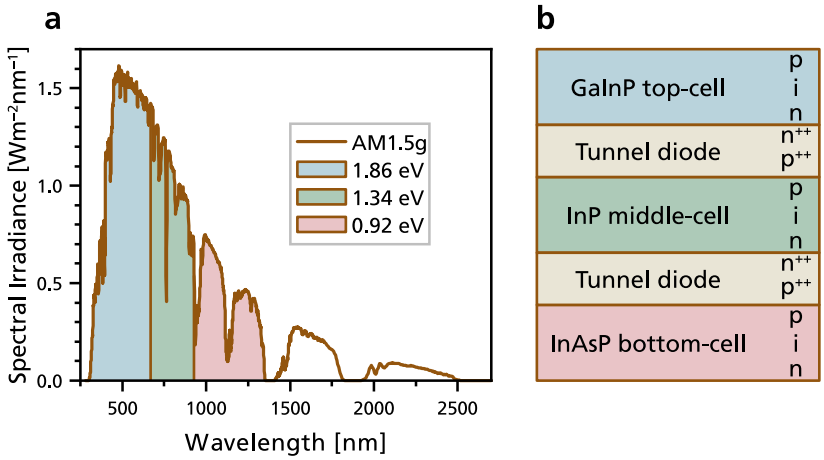

Figure 5.2: (a) Reference 1-Sun global spectrum (AM1.5g) from [205]. The wavelengths that can be absorbed by sub-cells with band gaps of 1.86 eV, 1.34 eV and 0.92 eV are colorized. (b) Schematic of a GaInP/InP/InAsP triple-junction solar cell. The materials and the order of doping represent the sample from Paper V.

While calculations show that the limit in efficiency for an infinite number of sub-cells is 68 %, or 86 % under concentrated light [206], the world record efficiency today is accomplished by a six-junction solar cell reaching 47.1 % under the direct spectrum (AM1.5d) under 143 suns concentration and 39.2 % under the one sun global spectrum (AM1.5g). Each sub-cell absorbs only part of the solar spectrum and therefore the generated current of a multi-junction solar cell is lower than the current of a single-junction solar cell. However, as the junctions are connected in series, the voltage of the multi-junction solar cell is the sum of the voltages generated by all sub-cells.

Depending on the number of junctions, the ideal band gaps for a multi-junction solar cell can be calculated but a further complication is to find semiconductors that not only have the correct band gap but also a matching lattice constant. Otherwise, defects from the mismatched layers can lead to recombination centers and traps for charge carriers and limit the efficiency. In ternary solid solutions of III–V semiconductors, the band gap can be continuously, though not linearly, adjusted between the band gaps of the two binary compounds as a function of the composition and thus, according to Vegard's law, to the lattice constant. Quaternary solid solutions on the other hand have an additional degree of freedom and therefore it is possible to independently adjust the band gap and the lattice constant at the same time. However, it is challenging to maintain a constant composition during epitaxy and the range in band gaps for a fixed lattice constant is not sufficient for multi-junction solar cells. Instead, world record multi-junction solar cells rely on so-called compositionally graded buffer layers. These layers are placed in-between two lattice mismatched sub-cells to relieve strain and confine misfit dislocations within inactive material [5].

Here, nanowires offer an alternative solution. Along the nanowire axis, materials with different lattice constants can be combined without strain-induced defects because of radial strain-relaxation. This simplifies the design of multi-junction solar cells, as the requirements for lattice-matching are eased.

5.1 Esaki Tunnel Diode

In order to connect the sub-cells of a multi-junction solar cell, Esaki tunnel diodes are used [207, 208]. Without a tunnel diode, a parasitic n–p junction is formed at the interface of two p–n junctions. This parasitic diode would limit the current and reduce the voltage of the multi-junction solar cell. Figure 5.3 schematically shows the *I–V* characteristics of a tunnel diode. In forward direction a characteristic negative differential resistance is observed. In this region, the tunneling current decreases and the exponentially increasing current in forward direction takes over. This increasing current is composed of the diffusion current and an excess current, which is mainly caused by tunneling through states within the band gap (Figure 5.3b). Important

parameters are the peak current I_P, the valley voltage V_V, and the peak-to-valley current ratio. It is easier to achieve tunnelling with a low band gap, but for multi-junction solar cells, the tunnel diode is desired to have a larger band gap than the subjacent sub-cell for optical transparency.

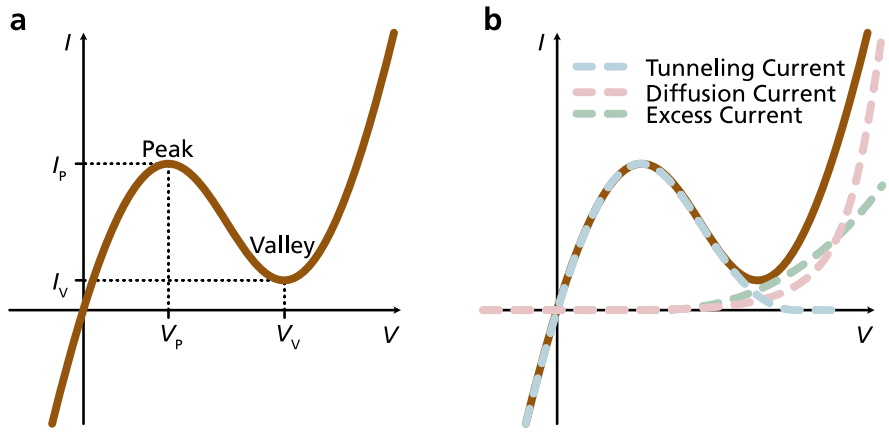

Figure 5.3: (a) Schematic current–voltage characteristics of a tunnel diode. (b) The current is the sum of three components: the tunneling current, the diffusion current, and an excess current. Adapted with permission from [209]. © 2007 John Wiley & Sons, Inc.

Figure 5.4 shows a schematic drawing of the band structure of a tunnel diode under different applied voltages. The tunnel diode is degenerately doped—*i.e.*, E_{Fn} is within the conduction band and E_{Fp} within the valence band for the n- and p-segment, respectively—and has a narrow depletion region. This results in a high conductivity in reverse direction, as electrons can tunnel from the valence band of the p-segment of the diode to the conduction band of the n-segment of the diode (Figure 5.4a). In forward direction, electrons can tunnel from the conduction band of the n-segment of the diode to the valence band of the p-segment of the diode. The tunneling current peaks at I_P (Figure 5.4c) and diminishes close to V_V (Figure 5.4d). At higher voltages, the diffusion and excess current dominate (Figure 5.4e).

In multi-junction solar cells, the tunnel diode is connected in backward direction to the solar cell. Under illumination, the solar cell generates a photocurrent. I_P of the tunnel diode should exceed I_{SC} generated by the solar cell. Otherwise—as the device is connected in series—a high voltage drops over the tunnel diode and a dip in the forward *I–V* characteristics of the solar cell appears (Figure 5.5), impairing the efficiency [210]. Esaki tunnel diodes have been demonstrated in nanowires both in axial [211-216] and in radial [217, 218] geometry. In Paper IV, three different axial Esaki tunnel diodes were synthesized and characterized.

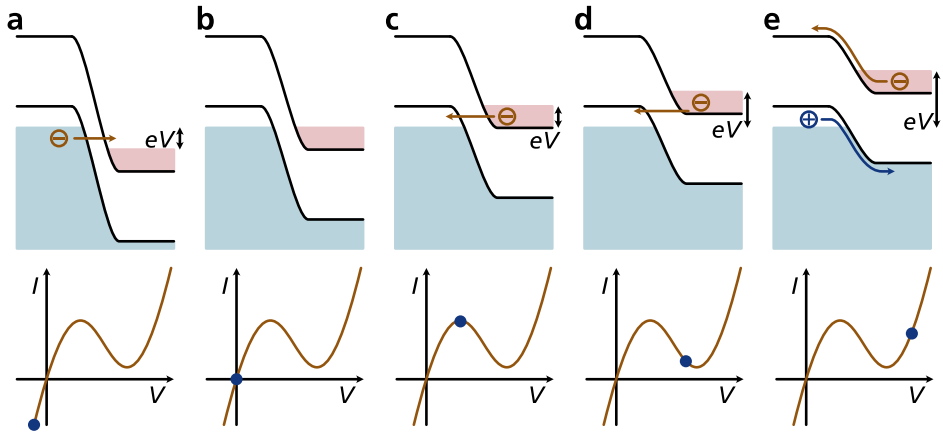

Figure 5.4: Schematic band diagram of a tunnel diode under different bias conditions. (a) At reverse bias, electrons tunnel from the valence band of the p^{++}-doped segment to the conduction band of the n^{++}-doped segment. (b) Without bias the diode is at thermal equilibrium and no current flows. (c) At forward bias, electrons tunnel from the conduction band of the n^{++}-doped segment to the valence band of the p^{++}-doped segment. (d) Approaching the valley voltage, the tunneling current diminishes. (e) At forward bias higher than the valley voltage the diffusion current is observed. Adapted with permission from [208]. © 1960 IEEE.

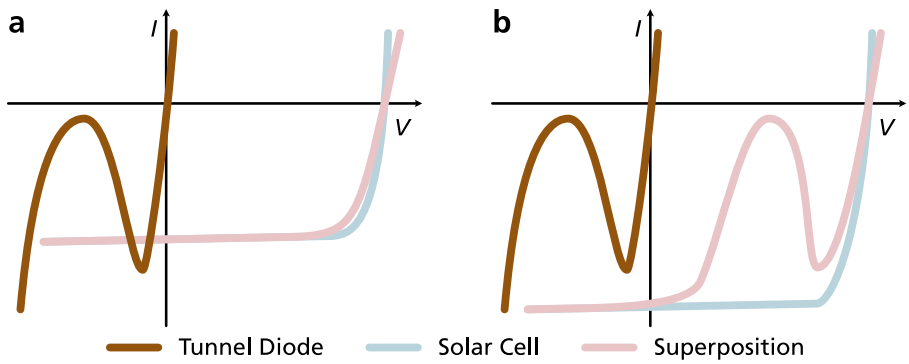

Figure 5.5: Schematic *I–V* characteristics under illumination of a tunnel diode, solar cell, and their superposition in a device connected in series. (a) If the absolute value of I_P is larger than the absolute value of I_{SC}, the tunnel diode operates at low voltage drops and acts as an ohmic resistance. (b) If the absolute value of I_P is smaller than the absolute value of I_{SC}, a high voltage drops over the tunnel diode at a small bias. At a larger bias, the voltage drop decreases. This results in a dip in the *I–V* characteristics of the device, producing a peak corresponding to I_P. Reproduced with permission from [210]. © 2006 IEEE.

5.2 Window Layer & Back-Surface-Field

In multi-junction solar cells, each sub-cell—in addition to the active p–n junction—is terminated by a window layer toward the front and a back-surface-field toward the back. These layers are highly doped and act as selective barriers for the minority charge carriers of the active region. Consequently, the interface recombination velocity is reduced [219]. Figure 5.6 shows a schematic band structure of a solar cell consisting of a p–i–n junction, a window layer, and a back-surface-field. The window layer and back-surface-field act as barriers for the minority charge carriers. In Paper IV, using a highly doped GaInP segment turned out to be crucial to prevent the formation of a parasitic diode when combining an n–i–p junction with an Esaki tunnel diode.

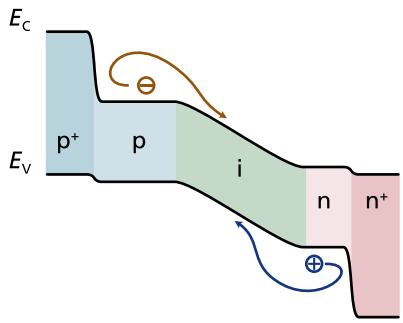

Figure 5.6: Schematic band diagram of a solar cell including a p–i–n junction, as well as a back-surface-field and a window layer. The back-surface-field and a window layer are highly doped and have a higher band gap than the p–i–n junction. The resulting offset in E_C acts as a barrier for electrons and the offset in E_V acts as a barrier for holes.

5.3 Sub-Cell Characterization

In order to optimize multi-junction solar cells, all sub-cells need to be fine-tuned. However, it is not trivial to measure the individual sub-cells of a multi-junction solar cell.

5.3.1 External Quantum Efficiency

Measuring the external quantum efficiency (EQE) of multi-junction solar cells can give insights into the performance of the individual sub-cells. In an EQE setup, a monochromator is used to measure the generated current of a solar cell as a function of the incident wavelength. A calibrated reference solar cell is measured to convert the

measured current to a quantum efficiency, *i.e.*, the fraction of incident photons that contribute to the photocurrent. This procedure is standardized for single-junction solar cells, but the measurement is more complicated for multi-junction solar cells. In general, a single wavelength would only excite one of the sub-cells of a multi-junction solar cell and the other sub-cells would limit the current. To get a response of an individual sub-cell, it has to be the current-limiting sub-cell and all other sub-cells need to be excited. This can be achieved by an external bias applied to the multi-junction solar cell.

An additional light source can act as an additional optical bias. If a dual-junction solar cell is illuminated by a long wavelength light source, only the bottom-cell is excited. This makes the top-cell the current-limiting sub-cell and an EQE measurements will represent the response of the top-cell. Similarly, if a short-wavelength light source is used to illuminate the dual-junction solar cell, most photons will be absorbed already in the top-cell. Therefore, the bottom-cell will limit the current—even though the photons would have enough energy to excite the bottom-cell—and its response can be measured.

Instead of using an additional light source, a voltage can be applied to the multi-junction solar cell as an electrical bias to measure the spectral response of a sub-cell. If a multi-junction solar cell is measured without an applied voltage, the sum of the operating voltage of all sub-cells is 0 V. However, the individual sub-cells are operating at different voltages. An optically biased top-cell will operate close to its V_{OC}. The bottom-cell thus has to operate at a similar voltage in reverse direction. Therefore, a voltage in forward direction needs to be applied to the multi-junction solar cell to measure the spectral response of the bottom-cell at open-circuit conditions. An electrical bias can thus be used to correct a shift of the operating voltage. However, this discussion changes, if one of the sub-cells has a low breakdown voltage [220]. In that case, if a voltage larger than the breakdown voltage of one sub-cell is applied, the spectral response of the other sub-cell can be obtained.

5.3.2 Biased Electron-Beam-Induced Current

While EBIC measurements are standard for single-junction solar cells, measuring multi-junction solar cells is not trivial. Few studies have been published, following the same strategy as optically biased EQE measurements, *i.e.*, using a light source as an optical bias to excite all sub-cells except for the one that is supposed to be analyzed [221, 222]. In general, two different measurement approaches are possible: top view and cross-sectional measurements. Top view measurements are useful to map defects, while cross-sectional measurements can be useful to estimate the diffusion length of charge carriers and the surface recombination velocity. In Paper IV, cross-sectional biased EBIC measurements have been used to individually characterize the sub-cells of

photovoltaic tandem-junction nanowires. In addition, by applying an electrical bias in forward direction, all sub-cells and tunnel diodes were measured in Papers IV and V.

5.4 Nanowire Multi-Junction Solar Cells

By utilizing multi-junction technology, world-record efficiencies have been accomplished in planar solar cells. However, the technology is too expensive for large area terrestrial applications. As nanowires absorb light from a larger area than their own cross-section, the material cost could be drastically reduced if the solar cell is made of nanowire arrays instead of continuous thin films.

5.4.1 Nanowires on Planar Solar Cell

One strategy to form a nanowire tandem-junction solar cell is to combine a nanowire solar cell with a planar solar cell [223]. The advantage of this approach is that the decade-long experience of conventional solar cells can be continued. The most obvious combination is to put III–V nanowires on top of a Si solar cell. The idea is to take existing, cheap solar cells and improve their efficiency by adding a top-cell. While this approach is possible for thin films too [224], the use of nanowires reduces the amount of necessary but expensive III–V material.

Such a hybrid nanowire/planar solar cell has been achieved using GaAs nanowires on top of Si(111) [225]. The tandem-junction reached a V_{OC} of 0.956 V, increasing the V_{OC} of the Si standalone solar cell by 0.438 V. Taking into account that the GaAs standalone solar cell reached a V_{OC} of 0.518 V, 89.8 % of the possible V_{OC} were obtained. However, in thin films, GaAs solar cells reach a V_{OC} of 1.127 V. Furthermore, the GaAs nanowire top-cell limited the current of the tandem device, leading to an overall efficiency of 11.4 %. Compared to the Si standalone solar cell, this corresponds to a mere increase of 2 % in power conversion efficiency. Besides the GaAs nanowire top-cell that is in need of optimization, this monolithic integration of III–V nanowires on Si depends on (111) wafer orientation. Standard Si solar cells, however, are made from (100) wafers.

Using a four-terminal instead of a monolithic two-terminal architecture, III–V nanowire solar cells could be combined with standard Si solar cells. The Swedish start-up Sol Voltaics AB patented the procedure to produce photovoltaic nanowires using a large scale aerotaxy technique [226, 227]. They had planned to subsequently align the nanowires in a film [228] to increase the efficiency of Si solar cells by up to 50 % [229, 230]. Unfortunately, the company could not deliver a finished product before becoming economically insolvent in 2019.

5.4.2 Radial Tandem-Junction Nanowires

Even though radial nanowire tandem-junction solar cells are limited by the same requirements of lattice-matching as thin films, a radial Si/SiGe nanowire tandem-junction solar cell was fabricated [231]. Remarkably, the device demonstrates flexibility and can be bent at a 10 mm radius, while at the same time having a record power-to-weight ratio of 1628 W/kg. On the other hand, the efficiency of the device is limited to 6.6 %. On aluminium-doped zinc oxide coated glass substrates, an efficiency of 8.1 % was achieved, which is still far below the efficiencies reached in single-junction nanowire solar cells. In addition to the lattice matching requirements, the radial design for multi-junction nanowires is limited in the number of junctions because the diameter of the nanowires is constrained by the distance between adjacent nanowires. Otherwise, with increasing distance between nanowires, less light would be absorbed.

5.4.3 Axial Tandem-Junction nanowires

Nanowires with an axial tandem-junction have been demonstrated both in Si nanowires [232], as well as InP nanowires [233]. In both cases, single nanowires were transferred to an insulating substrate and contacted by electron-beam lithography. In those lateral devices, addition of V_{OC} was demonstrated. However, in a vertical device, since both sub-cells are made from the same material, the top-cell would absorb most photons, leading to a severely limited bottom-cell. This again highlights the necessity to combine different band gaps.

6 Summary of Results

This chapter summarizes the experimental results of the publications this thesis is based on. In the Papers I-III single-junction nanowires are investigated. Paper I focuses on the synthesis of large area nanowire arrays for photovoltaics. Then, in Paper II oxides are deposited on nanowires and EBIC measurements are used to image the influence of the oxides on the electrostatic potential of the nanowires. Paper III describes a setup that combines a nanoprobe system with an optical fiber coupled to a multi-LED setup inside an SEM. With this setup, the *I–V* characteristics of single nanowires under *in situ* illumination were measured and correlated with EBIC measurements.

Guided by the multi-LED and EBIC setup, multi-junction nanowires were developed. Paper IV focuses on the development of tandem-junction nanowires. An optical and electrical bias was applied to individually measure the EBIC signal of both sub-cells. Finally, axially defined GaInP/InP/InAsP triple-junction photovoltaic nanowires optimized for light absorption exhibiting an open-circuit voltage of up to 2.37 V are described in Paper V. The open-circuit voltage amounts to 94 % of the sum of the respective single-junction nanowires.

6.1 Single-Junction Nanowires

6.1.1 Paper I

Single-junction nanowire solar cells have reached respectable efficiencies but so far only devices with areas of less than 1 mm^2 have been reported. In order to harvest light and generate significant amounts of electricity, large area nanowire arrays are needed. Paper I addresses this by demonstrating the synthesis of nanowire arrays on two inch wafers, paving the way to fabricate nanowire solar cells with areas in the order of cm^2. The wafers were then analyzed by using a PL mapper. PL spectra were measured throughout the wafer with a given step size, generating a 3D spectrum with the PL intensity as a function of X, Y, and λ. Furthermore, a similar map was measured for the PL decay, measuring the PL intensity as a function of X, Y, and t. To vertically process the nanowire arrays, it is important to know the length and diameter of the nanowires. Typically, this is measured using SEM. However, by using SEM only small areas can be

investigated—it would be too time-consuming to map out a full wafer. Besides, the focused electron beam of the SEM can deposit carbon on the sample which might have a negative effect on the final device. Therefore, it is interesting to measure the nanowire dimensions optically. In addition to a laser diode, the PL mapper can be operated with a white light source to measure the reflectance. As the reflectance of nanowire arrays is dependent on the length and diameter of the nanowires, the measured reflectance spectra can be utilized to extract the nanowire dimensions.

DTL was used to define the periodic pattern of the arrays. By changing the exposure dose during lithography, the feature size can be varied. Two wafers were prepared: Sample 1 was prepared by partly blocking the laser, defining five regions with different exposure doses on the same wafer to study nanowires with different diameters. Sample 2, on the other hand, was homogeneously patterned to demonstrate the scalability and study the homogeneity of the nanowire arrays over a large area. After lithography, Au evaporation, and lift-off, the patterned wafers were used to grow nanowires via the VLS mechanism. A PL mapper was used to map the reflectance of the wafers with a step size of 0.5 mm. The several thousand measured reflectance spectra were then compared with a database for the modeled reflectance spectra of nanowires with different diameters and lengths and a global fit was used to find the best-matching modeled spectrum. Thus, for every measured position on the wafer, the diameter and length of the nanowires in the array were extracted optically. Cross-sectional SEM measurements within the five regions of Sample 1 confirmed the results of the optical extraction. Figure 6.1 shows a photograph of Sample 1 and an SEM image of the central region (left), as well as a plot of the extracted lengths and diameters, color-coded to the five regions.

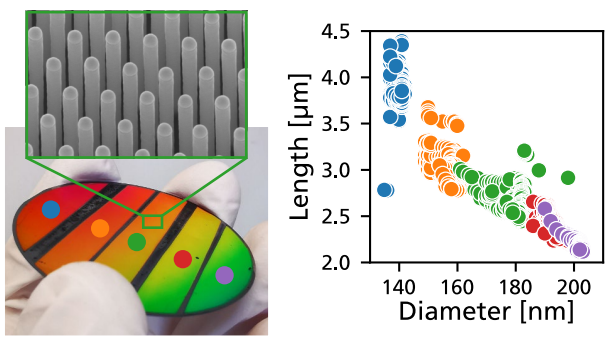

Figure 6.1: Photograph of Sample 1 with five separate regions of different exposure dose. The SEM image shows the nanowires in the center of the wafer. By mapping the reflectance spectra, the length and diameter of the nanowires was extracted for several thousand positions on the wafer. Reproduced from Paper I.

As expected, the regions with higher exposure dose on Sample 1 resulted in nanowires with larger diameter. As the pitch of the arrays is constant, and the same precursor flux

arrives at the wafer, a larger nanowire diameter results in a shorter length during nanowire synthesis because the volume of the grown crystals should stay constant. At the edges, both at the edge of the wafer and at the edge of the pre-defined regions, the nanowires are longer. This edge effect is a consequence of adjacent inactive areas within the diffusion length of the precursors such as the susceptor. Additionally, the homogenously patterned Sample 2—while the diameter of the nanowires is basically constant—exhibits a radial gradient for the length of the nanowires that peaks at the center of the wafer. This effect has previously not been observed in smaller samples and can be attributed to a gradient in the MOVPE reactor, either in temperature of the susceptor, or in the effective precursor flux arriving at the wafer.

Maps of the PL intensity and TRPL lifetime show a similar gradient, resulting in higher intensities and longer lifetimes at the center of the wafers. This implies an improved crystal quality of the nanowires in the center of the wafer.

6.1.2 Paper II

Due to their geometry, nanowires have a high surface-to-volume ratio. At the surface, where the periodicity of the crystal is interrupted, recombination centers such as dangling bonds can increase the surface recombination velocity which impairs the efficiency of solar cells. The native oxide of InP nanowires leads to a low surface recombination velocity compared to other III–V semiconductors, resulting in the highest efficiencies among nanowire solar cells. Still, during the fabrication of nanowire solar cells, the nanowire surface can be affected by the processing steps. Typically, a transparent oxide is deposited by ALD to electrically insulate the p–n junction. Ideally, this oxide passivates the semiconductor surface but in many cases a deterioration in charge carrier lifetimes has been reported. The choice of insulating oxide is crucial, but even the deposition method can affect the performance of the nanowires. Otnes *et al.* reported on nanowire solar cells processed with SiO_2 as insulating layer, which was deposited using two different ALD reactors, resulting in a significant difference in the power conversion efficiency of the processed devices [124].

However, even the oxide that led to higher efficiencies decreases the PL intensity of InP nanowires. Another oxide, PO_x, has been shown to increase the PL decay lifetime for InP nanowires [159]. PO_x is hygroscopic and reacts with water present in the air to phosphorous acid (in the case of P_4O_6) and phosphoric acid (in the case of P_4O_{10}). Therefore, it needs to be protected by an Al_2O_3 layer. The same combination of oxides has also been reported to contain fixed positive charges [234]. In addition to the chemical passivation of the nanowire surface, static charges in the passivation layer have to be considered as they can cause a field-effect which affects the electrostatic potential of nanowires via remote doping [162].

In Paper II such a field-effect was directly imaged by using EBIC measurements. InP nanowire p–i–n junctions were synthesized with varying carrier concentrations in the middle segment. Lack of intentional doping results in n-type nanowires due to P-vacancies. Low concentrations of a p-dopant result in compensation doped nanowires and higher concentrations result in p-type nanowires. In addition to as-grown samples, two different oxides were deposited—SiO_x and PO_x/Al_2O_3. The piezo-controlled tungsten probe was used inside an SEM to penetrate the oxide layer and contact the seed particle of the VLS grown nanowires. The EBIC profiles along nanowires with nominally intrinsic, compensation doped, and overcompensation doped middle segment are shown in Figure 6.2a-c, respectively. A compensation doped middle segment results in a relatively flat EBIC profile for as-grown nanowires with a peak at the i–n interface, indicating that the middle segment is slightly p-doped. The EBIC profile is hardly affected by the SiO_x layer, although a drop in the EBIC signal was observed. The PO_x/Al_2O_3 layer on the other hand exhibits an additional peak at the p–i interface. This new peak appears because of the field-effect induced by the fixed positive charges in the PO_x layer, which results in an inversion of the middle segment from slightly p-doped to slightly n-doped.

The effect of the oxides on the electrostatic potential of the nanowires has implications on the ideal doping level of the middle segment of nanowire p–i–n junctions. For SiO_x, it is crucial to have high control over the doping level, as p–i–n junctions with both too much and too little doping in the middle segment result in an inferior p–i–n junction after the deposition of SiO_x. The fixed charges in the PO_x/Al_2O_3 layer increase the margin and it becomes favorable to overcompensate the middle segment during nanowire synthesis.

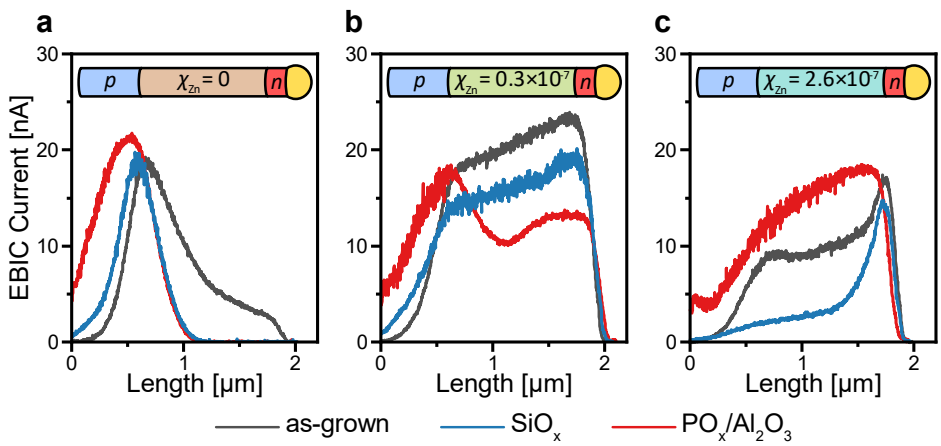

Figure 6.2: Representative EBIC profiles along the NW axes including the Au particle. The DEZn molar fraction in the middle segment is increased from (a) $\chi_{Zn} = 0$, to (b) $\chi_{Zn} = 0.3 \times 10^{-7}$ to (c) $\chi_{Zn} = 2.6 \times 10^{-7}$. PO_x/Al_2O_3 induces an n-type field-effect that moves the peak position of the EBIC signal for all samples. SiO_x decreases the EBIC signal in the middle segments but increases the EBIC signal in the p-segment of the NWs. Reproduced from Paper II.

6.1.3 Paper III

Measuring the EBIC and dark *I–V* characteristics of single photovoltaic nanowires inside an SEM using piezo-controlled tungsten probes has proven useful to obtain rapid feedback after nanowire synthesis. In a processed solar cell, the intention is to convert light into electricity instead of a focused electron beam. Therefore, it is important to be able to measure the *I–V* characteristics under illumination. In Paper III, a setup is described that combines a piezo-controlled prober shuttle with a multi-LED coupled inside an SEM by an optical fiber. Four different single-wavelength LEDs can be used individually or in combination to illuminate samples inside the SEM. Alternatively, a fifth LED emitting a warm white light (4000 K) can be used. Figure 6.3a shows the normalized spectral characteristics of the five LEDs.

Already in Paper II it was argued that a flat EBIC profile along the nanowires is desired as this maximizes the probability to separate charge carriers and generating current. In Paper III, nanowires with a similar variation in the doping level of the middle segment of a p–i–n junction are illuminated with LEDs to show that higher EBIC profiles correlate with an increase in I_{SC}.

The illumination intensity can be adjusted by changing the distance of the optical fiber to the sample and the operation current of the LEDs. Thereby, the I_{SC} of a single InP nanowire was varied over four orders of magnitude (Figure 6.3b). This was utilized to study the *I–V* characteristics of single nanowires under light concentration. In a processed nanowire solar cell current densities of 25 mA/cm^2 are reached [124], corresponding to a current of 54 pA per nanowire for a hexagonal pattern with a pitch of 500 nm. With the LED setup, a maximum I_{SC} of 8 nA was measured for a single nanowire, about 150 times more current than expected to be generated at one sun illumination. Over the four orders of magnitudes that I_{SC} was varied, V_{OC} changed as expected (Figure 6.3c).

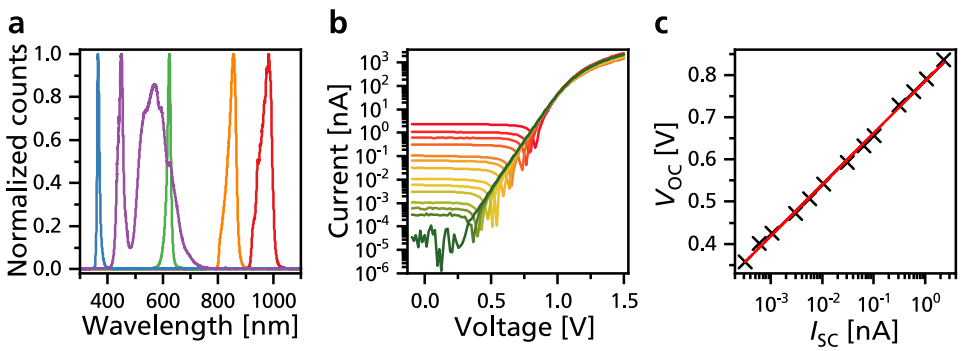

Figure 6.3: (a) Normalized spectral characteristics of the available LEDs. (b) *I–V* characteristics of a single InP nanowire under varying light intensities. (c) V_{OC} evolution with the different irradiance levels achieved in (b). Reproduced from Paper III.

6.2 Multi-Junction Nanowires

EBIC has been used extensively to characterize photovoltaic single-junction nanowires, but it has also been essential to develop tandem-junction nanowires, as described in Paper IV. The multi-LED setup described in Paper III was used to apply an optical bias during EBIC measurements of tandem-junction nanowires, enabling the characterization of the individual sub-cells. The gathered know-how of the tandem-junction development culminated in Paper V in which the realization of photovoltaic GaInP/InP/InAsP triple–junction nanowires with a measured V_{OC} of up to 2.37 V is reported.

6.2.1 Paper IV

In order to synthesize photovoltaic tandem-junction nanowires, two sub-cells with different band gaps need to be connected by an Esaki tunnel diode. Three different p^{++}–n^{++} tunnel diodes were synthesized based on highly doped homojunctions of InP and GaInP, and a GaInP/InP heterojunction. Even though all samples exhibited the typical negative differential resistance of an Esaki tunnel diode, the peak current of the GaInP homojunction was substantially lower. The InP homojunction on the other hand had the longest depletion width because of the p^{++}-doped InP segment.

When combining an InP n–i–p junction with a p^{++}–n^{++} InP tunnel diode, a parasitic junction was measured with EBIC. This is seen as an additional peak in the EBIC measurement in reverse direction. This could be attributed to the long depletion width within the p^{++}-doped InP. However, increasing the length of this segment to separate the two diodes did not prevent the formation of a parasitic junction. Using the GaInP/InP heterojunction tunnel diode prevents the formation of a parasitic junction and the n–i–p–p^{++}–n^{++} sample behaves like an n–i–p junction, proving the electrical transparency of the tunnel diode. The reason for the successful combination using the GaInP/InP heterojunction is not only the shorter depletion width of the tunnel diode. If only the GaInP segment is added—resulting in an n–i–p–p^{++} sample—the EBIC signal within the InP sub-cell is increased. This indicates that the GaInP segment acts as a selective barrier for minority carriers, similarly to the window layers used in multi-junction solar cells.

Finally, a GaInP top-cell was added, resulting in n–i–p–p^{++}–n^{++}–n–i–p GaInP/InP tandem-junction nanowires, as schematically drawn in Figure 6.4a. EBIC measurements without additional bias could not be used for characterization because only one of the sub-cells would be excited at a time, with the other sub-cell limiting the current. Therefore, an additional bias needed to be applied, exciting one of the sub-cells to measure the other, current-limiting sub-cell using EBIC. To saturate the bottom-cell, the tandem-junction nanowire can be illuminated by a light source that is mostly

absorbed by the bottom-cell. This makes the top-cell the current-limiting cell and it can be characterized individually using EBIC (Figure 6.4b). To characterize the bottom-cell of planar multi-junction solar cells, the top-cell is typically saturated with UV light. This approach does not work for cross-sectional analysis, as UV light would be absorbed by all sub-cells. Therefore, an electrical bias in reverse direction larger than the breakdown voltage of the top-cell was used to saturate the top-cell to characterize the bottom-cell individually (Figure 6.4c). With both an electrical and an optical bias applied, the two sub-cells could be measured simultaneously (Figure 6.4d).

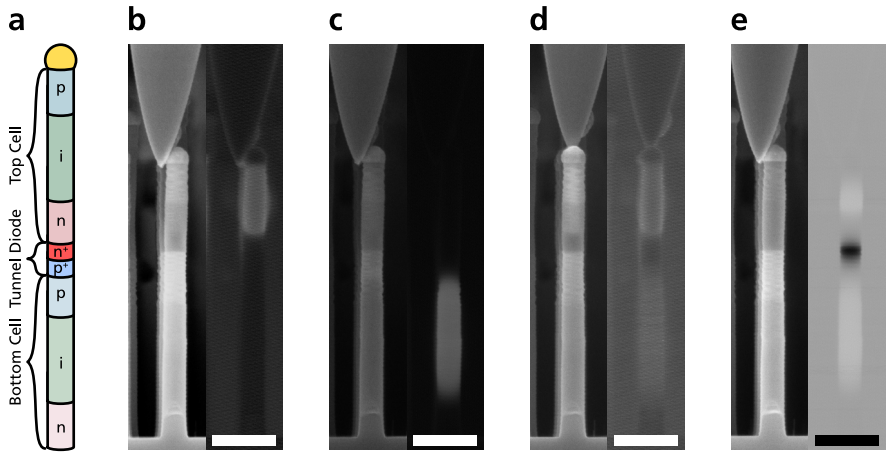

Figure 6.4: (a) Schematic of an axial VLS grown tandem-junction nanowire. (b,c,d,e) SEM (left) and EBIC (right) images of the same NW under different conditions. (b) Without applied electrical bias but with optical bias from the LED source. (c) With applied electrical bias in reverse direction but without optical bias. (d) With both applied electrical bias in reverse direction and optical bias. (e) With applied electrical bias in forward direction. Reproduced from Paper IV.

In addition to the GaInP/InP tandem-junction nanowires, InP/InAsP nanowires were synthesized. Using an optical bias, the InP top-cell could be characterized using EBIC, however, the breakdown voltage of the InP top-cell appeared to be higher than −10 V, the limit of the used EBIC amplifier. As an alternative, an electrical bias in forward direction close to V_{OC} was applied. In that case, all junctions, both sub-cells and the tunnel diode can be measured simultaneously, with the tunnel diode appearing as a peak with opposite sign than the sub-cells (Figure 6.4e).

6.2.2 Paper V

Conventional multi-junction solar cells are either constrained to lattice matched materials, such as in the $Ga_{0.5}In_{0.5}P$/GaAs/Ge material system, or depend on methods to combine lattice mismatched materials, such as compositionally graded buffer layers

or wafer bonding. In nanowires, lattice mismatched materials can be combined along the nanowire axis without the formation of strain-induced defects.

Assuming InP with a band gap of 1.34 eV as the middle-cell in a triple-junction solar cell, the ideal band gaps for the bottom-cell and top-cell are 0.92 eV and 1.86 eV, respectively. These values are accessible in $InAs_xP_{1-x}$ and $Ga_xIn_{1-x}P$. This combination of band gaps has the potential to reach a power conversion efficiency of 47 %. Such GaInP/InP/InAsP triple-junction nanowires, as depicted in Figure 6.5a, were realized in Paper V. XRD was used to determine the composition via Vegard's law, which was confirmed by spatially resolved EDXS. As described in Paper IV, an electrical bias was applied in forward direction to measure the EBIC signal of all three sub-cells and the two Esaki tunnel diodes (Figure 6.5b).

In addition to the triple-junction nanowires, single-junction nanowires with the material composition and doping profile from the three sub-cells were synthesized. The *I–V* characteristics of the single-junction nanowires demonstrate that a high band gap results in a high voltage due to the larger difference in the chemical potential of the charge carriers, but in a low current as fewer photons can be absorbed (Figure 6.5c). Consequently, due to the cross-sectional illumination during the single nanowire measurements, the current of the triple-junction nanowires is limited by the GaInP top-cell. However, this situation might be different in a vertically processed device in which the sub-cells are not illuminated by the full spectrum, but only by the filtered spectrum that is transmitted through the above sub-cells. The average V_{OC} of the triple-junction nanowires amounts to 94 % of the sum of the average V_{OC} of the single-junction nanowires and the highest measured V_{OC} of the triple-junction—2.37 V—corresponds to the same value as by adding the highest measured V_{OC} of the single junctions within the measurement error.

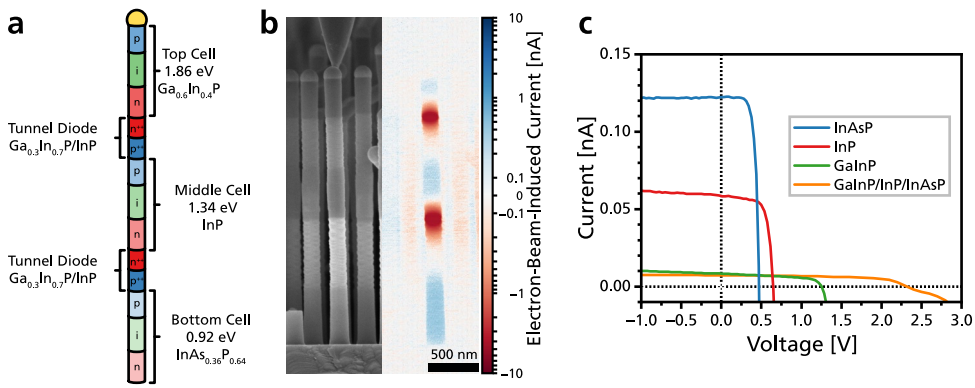

Figure 6.5: (a) Schematic of an axial VLS grown triple-junction nanowire. (b) SEM (left) and EBIC (right) images of a triple-junction nanowire under electrical bias in forward direction. (c) Illuminated *I–V* characteristics of InAsP, InP, and GaInP single-junction nanowires and a GaInP/InP/InAsP triple-junction nanowire. Reproduced from Paper V.

7 Outlook

The focus of the experimental work of this thesis has been to synthesize ordered arrays of photovoltaic multi-junction nanowires and to find a suitable method to characterize their properties on a single nanowire level. By using a piezo-controlled prober shuttle, single nanowire *I*–*V* characteristics and electron-beam-induced current measurements have been utilized to investigate photovoltaic nanowires.

7.1 Processing of Nanowire Multi-Junction Solar Cells

The intention of combining several sub-cells to a multi-junction solar cell is to increase the power conversion efficiency. Although single nanowire measurements are a proof of concept and indeed confirm V_{OC} addition, to measure an efficiency, a processed solar cell is needed. While the processing itself is very similar to the processing of a single-junction solar cell, it is to be expected that more optimization is necessary to achieve high efficiencies, both regarding nanowire synthesis, as well as subsequent processing to devices.

7.1.1 Current Matching

One aspect that needs to be considered is current matching. The sub-cell with the lowest current will limit the current of the multi-junction solar cell. While the GaInP top-cell is current-limiting in the single nanowire measurements, it is not trivial that this has to be the same case in a processed device. The difference is that the single nanowires are not illuminated from the top but from the cross-section. From the cross-section, all sub-cells are illuminated with the same light source but in a processed device each sub-cell is absorbing light, altering the incident light source of the subjacent sub-cells.

To increase the current, it will presumably be necessary to passivate the surface of the current-limiting sub-cell. InP is known to have a low surface recombination velocity compared to other III–V semiconductors, but for the other sub-cells the surface might be the limiting factor. The easiest approach would be to find a suitable dielectric that is able to passivate the surface of all sub-cells via atomic layer deposition. If no suitable material can be found, epitaxial passivation might be considered. However, while it is

relatively easy to combine materials with different lattice constants along the nanowire axis, an epitaxially grown shell can only be lattice-matched to one of the sub-cells and would induce strain in the other sub-cells. In theory, it would be possible to use a multi-step growth to combine axial junctions with radial passivation similar to the design in Ref [176], but in practice such an approach would be extremely challenging.

7.1.2 Considerations Regarding Growth Direction

During the processing, a transparent front contact to the nanowires needs to be formed. Typically, indium tin oxide (ITO) or other transparent conductive oxides (TCO) are used. However, most TCOs are n-type contacts. Therefore, it would be convenient to terminate the nanowire synthesis with an n-segment. Unfortunately, forming an Esaki tunnel diode is significantly more difficult in n–p direction than vice versa because the Zn used for p-doping needs to accumulate in the growth chamber and in the seed droplet until sufficiently high doping can be reached. In p–n direction, even though the accumulated Zn in the seed droplet causes a reservoir effect, using S as n-dopant, sufficiently high concentration can be reached to form a tunnel diode. Consequently, the Esaki tunnel diode is currently limiting the doping order of the sub-cells. This leads to a p-type top segment, although an additional tunnel diode could be used to terminate with an n-type segment.

While some reports exist using MoO_x as a hole-selective contact [170, 235-239], initial experiments in our group led to challenges in the processing of devices as (i) it is important to prevent oxidation of the suboxide because stoichiometric MoO_3 is not conductive, and (ii) MoO_x is easily etched by HCl, which is used to define the device area [240]. Fortunately, ITO seems to be a good contact to p-type InP but at some point, the front contact might become one of the factors limiting the efficiency of a processed multi-junction solar cell.

If future work to fabricate sufficiently conductive tunnel diodes in n–p direction continues to be challenging, an alternative solution for an n-type front contact could be to add another tunnel diode on top of the top-cell. Another degree of freedom is obtained if the nanowires are removed from the substrate and flipped to fabricate the front contact on the bottom of the nanowires. In that case the doping order can remain as it is in the current design, although the order of the sub-cells needs to be reversed.

7.2 Nanowire Peel-Off

In order to remove the nanowires from their native substrate, the nanowire array is typically embedded in a polymer and subsequently peeled-off from the growth substrate. Often, a very thick layer of polydimethylsiloxane (PDMS) is used [241-244],

but this material is difficult to further process. An elegant way to achieve peeled-off nanowire arrays is to use a double exposure technique combining positive and negative resists, as described in Paper VIII. However, so far this method is limited to small areas. Once sufficiently large areas of the nanowire arrays can be peeled-off, it would not only open the door to reverse the sub-cell order as described previously, but also to fabricate flexible and semi-transparent devices.

Furthermore, if peeled-off nanowire arrays can be processed to useful devices, the substrate can be re-used several times to grow new nanowire arrays [241, 245, 246]. Reusing the expensive III–V semiconductor growth substrate would significantly reduce the cost of nanowire solar cells.

References

1. IEA. *Electricity Market Report - July 2021, IEA, Paris* 2021; Available from: https://www.iea.org/reports/electricity-market-report-july-2021.
2. BP. *Statistical Review of World Energy*. 2021; Available from: https://www.bp.com/content/dam/bp/business-sites/en/global/corporate/pdfs/energy-economics/statistical-review/bp-stats-review-2021-full-report.pdf.
3. IPCC, *Climate Change 2021: The Physical Science Basis. Contribution of Working Group I to the Sixth Assessment Report of the Intergovernmental Panel on Climate Change*, V. Masson-Delmotte, et al., Editors. 2021: Cambridge University Press. In Press.
4. Morton, O., *Solar energy: a new day dawning? Silicon Valley sunrise.* Nature, 2006. **443**(7107): p. 19-22.
5. Geisz, J.F., et al., *Six-junction III–V solar cells with 47.1% conversion efficiency under 143 Suns concentration.* Nature Energy, 2020. **5**(4): p. 326-335.
6. Horowitz, K.A., et al. *A Techno-Economic Analysis and Cost Reduction Roadmap for III-V Solar Cells*. 2018; Available from: https://doi.org/10.2172/1484349.
7. Sun, J. and Jasieniak, J.J., *Semi-transparent solar cells.* Journal of Physics D-Applied Physics, 2017. **50**(9).
8. Oregan, B. and Grätzel, M., *A Low-Cost, High-Efficiency Solar-Cell Based on Dye-Sensitized Colloidal TiO_2 Films.* Nature, 1991. **353**(6346): p. 737-740.
9. Hagfeldt, A., et al., *Dye-Sensitized Solar Cells.* Chemical Reviews, 2010. **110**(11): p. 6595-6663.
10. Green, M.A., Ho-Baillie, A., and Snaith, H.J., *The emergence of perovskite solar cells.* Nature Photonics, 2014. **8**(7): p. 506-514.
11. Stranks, S.D. and Snaith, H.J., *Metal-halide perovskites for photovoltaic and light-emitting devices.* Nature Nanotechnology, 2015. **10**(5): p. 391-402.
12. Garnett, E.C., et al., *Nanowire Solar Cells.* Annual Review of Materials Research, 2011. **41**(1): p. 269-295.
13. LaPierre, R.R., et al., *III–V nanowire photovoltaics: Review of design for high efficiency.* Physica Status Solidi-Rapid Research Letters, 2013. 7(10): p. 815-830.
14. Otnes, G. and Borgström, M.T., *Towards high efficiency nanowire solar cells.* Nano Today, 2017. **12**: p. 31-45.
15. Barrigón, E., et al., *Synthesis and Applications of III–V Nanowires.* Chemical Reviews, 2019. **119**(15): p. 9170-9220.
16. Hu, J.T., Odom, T.W., and Lieber, C.M., *Chemistry and Physics in One Dimension: Synthesis and Properties of Nanowires and Nanotubes.* Accounts of Chemical Research, 1999. **32**(5): p. 435-445.

17. Rao, C.N.R., et al., *Inorganic nanowires.* Progress in Solid State Chemistry, 2003. **31**(1-2): p. 5-147.
18. Law, M., Goldberger, J., and Yang, P., *Semiconductor Nanowires and Nanotubes.* Annual Review of Materials Research, 2004. **34**(1): p. 83-122.
19. Lu, W. and Lieber, C.M., *Semiconductor nanowires.* Journal of Physics D-Applied Physics, 2006. **39**(21): p. R387-R406.
20. Sears, G.W., *A Growth Mechanism for Mercury Whiskers.* Acta Metallurgica, 1955. **3**(4): p. 361-366.
21. Wagner, R.S. and Ellis, W.C., *Vapor-Liquid-Solid Mechanism of Single Crystal Growth.* Applied Physics Letters, 1964. **4**(5): p. 89-90.
22. Bootsma, G.A. and Gassen, H.J., *A quantitative study on the growth of silicon whiskers from silane and germanium whiskers from germane.* Journal of Crystal Growth, 1971. **10**(3): p. 223-234.
23. Yazawa, M., et al., *Effect of one monolayer of surface gold atoms on the epitaxial growth of InAs nanowhiskers.* Applied Physics Letters, 1992. **61**(17): p. 2051-2053.
24. Yazawa, M., et al., *Semiconductor Nanowhiskers.* Advanced Materials, 1993. **5**(7-8): p. 577-580.
25. Björk, M.T., et al., *One-dimensional heterostructures in semiconductor nanowhiskers.* Applied Physics Letters, 2002. **80**(6): p. 1058-1060.
26. Xia, Y.N., et al., *One-Dimensional Nanostructures: Synthesis, Characterization, and Applications.* Advanced Materials, 2003. **15**(5): p. 353-389.
27. Seifert, W., et al., *Growth of one-dimensional nanostructures in MOVPE.* Journal of Crystal Growth, 2004. **272**(1-4): p. 211-220.
28. Barth, S., et al., *Synthesis and applications of one-dimensional semiconductors.* Progress in Materials Science, 2010. **55**(6): p. 563-627.
29. Lauhon, L.J., et al., *Epitaxial core–shell and core–multishell nanowire heterostructures.* Nature, 2002. **420**(6911): p. 57-61.
30. Dick, K.A., et al., *Growth of GaP nanotree structures by sequential seeding of 1D nanowires.* Journal of Crystal Growth, 2004. **272**(1-4): p. 131-137.
31. Gazibegovic, S., et al., *Epitaxy of advanced nanowire quantum devices.* Nature, 2017. **548**(7668): p. 434-438.
32. Fowlkes, J.D., et al., *Simulation-Guided 3D Nanomanufacturing via Focused Electron Beam Induced Deposition.* ACS Nano, 2016. **10**(6): p. 6163-72.
33. Wan, Q., et al., *Fabrication and ethanol sensing characteristics of ZnO nanowire gas sensors.* Applied Physics Letters, 2004. **84**(18): p. 3654-3656.
34. Wang, Z.L. and Song, J., *Piezoelectric Nanogenerators Based on Zinc Oxide Nanowire Arrays.* Science, 2006. **312**(5771): p. 242-246.
35. Wang, Z.L., *Triboelectric Nanogenerators as New Energy Technology for Self-Powered Systems and as Active Mechanical and Chemical Sensors.* ACS Nano, 2013. **7**(11): p. 9533-9557.
36. McIntyre, P.C. and Fontcuberta i Morral, A., *Semiconductor nanowires: to grow or not to grow?* Materials Today Nano, 2020. **9**.
37. Yoo, J., et al., *Epitaxial growth of radial Si p-i-n junctions for photovoltaic applications.* Applied Physics Letters, 2013. **102**(9).

38. de la Mata, M., et al., *Atomic Scale Strain Relaxation in Axial Semiconductor III–V Nanowire Heterostructures.* Nano Letters, 2014. **14**(11): p. 6614-6620.
39. Eigler, D.M. and Schweizer, E.K., *Positioning single atoms with a scanning tunnelling microscope.* Nature, 1990. **344**(6266): p. 524-526.
40. Johnson, B.C., McCallum, J.C., and Aziz, M.J., *Solid-Phase Epitaxy*, in *Handbook of Crystal Growth*. 2015. p. 317-363.
41. Mauk, M.G., *Liquid-Phase Epitaxy*, in *Handbook of Crystal Growth*. 2015. p. 225-316.
42. Ptak, A.J., *Principles of Molecular Beam Epitaxy*, in *Handbook of Crystal Growth*. 2015. p. 161-192.
43. Fujioka, H., *Pulsed Laser Deposition (PLD)*, in *Handbook of Crystal Growth*. 2015. p. 365-397.
44. Choy, K.L., *Chemical vapour deposition of coatings.* Progress in Materials Science, 2003. **48**(2): p. 57-170.
45. Pohl, U.W., *Epitaxy of Semiconductors*. Graduate Texts in Physics. 2013.
46. Stringfellow, G.B., *Organometallic Vapor-Phase Epitaxy*. 1999: Academic Press.
47. Rothfuss, P., *The Name of the Wind*. 2008, Orion Publishing Group. p. 420.
48. Cowley, A.H. and Jones, R.A., *Single-Source III/V Precursors - a New Approach to Gallium-Arsenide and Related Semiconductors.* Angewandte Chemie-International Edition in English, 1989. **28**(9): p. 1208-1215.
49. Sun, L., et al., *Chemical vapour deposition.* Nature Reviews Methods Primers, 2021. **1**(1).
50. Frank, F.C. and van der Merwe, J.H., *One-dimensional dislocations. I. Static theory.* Proceedings of the Royal Society of London. Series A. Mathematical and Physical Sciences, 1949. **198**(1053): p. 205-216.
51. Frank, F.C. and van der Merwe, J.H., *One-dimensional dislocations. II. Misfitting monolayers and oriented overgrowth.* Proceedings of the Royal Society of London. Series A. Mathematical and Physical Sciences, 1949. **198**(1053): p. 216-225.
52. Frank, F.C. and van der Merwe, J.H., *One-dimensional dislocations - III. Influence of the second harmonic term in the potential representation, on the properties of the model.* Proceedings of the Royal Society of London. Series A. Mathematical and Physical Sciences, 1949. **200**(1060): p. 125-134.
53. Volmer, M. and Weber, A., *Keimbildung in übersättigten Gebilden.* Zeitschrift für Physikalische Chemie, 1926. **119U**(1): p. 277-301.
54. Stranski, I.N. and Krastanow, L., *Zur Theorie der orientierten Ausscheidung von Ionenkristallen aufeinander.* Monatshefte für Chemie, 1937. **71**(1): p. 351-364.
55. Osipov, A.V., et al., *Stress-driven nucleation of coherent islands: theory and experiment.* Applied Surface Science, 2002. **188**(1-2): p. 156-162.
56. Dubrovskii, V.G., *Nucleation Theory and Growth of Nanostructures*. NanoScience and Technology. 2014: Springer, Berlin, Heidelberg.
57. Kawai, H., et al., *Complex refractive indices of AlGaAs at high temperatures measured by in situ reflectometry during growth by metalorganic chemical vapor deposition.* Journal of Applied Physics, 1987. **61**(1): p. 328-332.
58. Irvine, S.J.C. and Bajaj, J., *A study of the growth kinetics of II–VI metalorganic vapour phase epitaxy using in situ laser reflectometry.* Journal of Crystal Growth, 1994. **145**(1-4): p. 74-81.

59. Heurlin, M., et al., *In Situ Characterization of Nanowire Dimensions and Growth Dynamics by Optical Reflectance.* Nano Letters, 2015. **15**(5): p. 3597-3602.
60. Anttu, N., et al., *Optical Far-Field Method with Subwavelength Accuracy for the Determination of Nanostructure Dimensions in Large-Area Samples.* Nano Letters, 2013. **13**(6): p. 2662-2667.
61. Schulz, M., *Determination of Deep Trap Levels in Silicon Using Ion-Implantation and CV-Measurements.* Applied Physics, 1974. **4**(3): p. 225-236.
62. Allen, J.E., et al., *High-resolution detection of Au catalyst atoms in Si nanowires.* Nature Nanotechnology, 2008. **3**(3): p. 168-173.
63. Putnam, M.C., et al., *Secondary Ion Mass Spectrometry of Vapor–Liquid–Solid Grown, Au-Catalyzed, Si Wires.* Nano Letters, 2008. **8**(10): p. 3109-3113.
64. Okamoto, H. and Massalski, T.B., *The Au–Si (Gold-Silicon) system.* Bulletin of Alloy Phase Diagrams, 1983. **4**(2): p. 190-198.
65. Wang, Y., et al., *Epitaxial growth of silicon nanowires using an aluminium catalyst.* Nature Nanotechnology, 2006. **1**(3): p. 186-189.
66. Wang, F., et al., *Solution–Liquid–Solid Growth of Semiconductor Nanowires.* Inorganic Chemistry, 2006. **45**(19): p. 7511-7521.
67. Wang, J., et al., *Solution–Solid–Solid Mechanism: Superionic Conductors Catalyze Nanowire Growth.* Nano Letters, 2013. **13**(9): p. 3996-4000.
68. Hanrath, T. and Korgel, B.A., *Supercritical Fluid–Liquid–Solid (SFLS) Synthesis of Si and Ge Nanowires Seeded by Colloidal Metal Nanocrystals.* Advanced Materials, 2003. **15**(5): p. 437-440.
69. Tuan, H.Y., et al., *Catalytic Solid-Phase Seeding of Silicon Nanowires by Nickel Nanocrystals in Organic Solvents.* Nano Letters, 2005. **5**(4): p. 681-684.
70. Ross, F.M., Tersoff, J., and Reuter, M.C., *Sawtooth Faceting in Silicon Nanowires.* Physical Review Letters, 2005. **95**(14): p. 146104.
71. Ross, F.M., *Controlling nanowire structures through real time growth studies.* Reports on Progress in Physics, 2010. **73**(11).
72. Kodambaka, S., et al., *Germanium Nanowire Growth Below the Eutectic Temperature.* Science, 2007. **316**(5825): p. 729-732.
73. Hofmann, S., et al., *Ledge-flow-controlled catalyst interface dynamics during Si nanowire growth.* Nature Materials, 2008. 7(5): p. 372-375.
74. Gamalski, A.D., Ducati, C., and Hofmann, S., *Cyclic Supersaturation and Triple Phase Boundary Dynamics in Germanium Nanowire Growth.* Journal of Physical Chemistry C, 2011. **115**(11): p. 4413-4417.
75. Motohisa, J., et al., *Catalyst-free selective-area MOVPE of semiconductor nanowires on (111)B oriented substrates.* Journal of Crystal Growth, 2004. **272**(1-4): p. 180-185.
76. Yeh, C.Y., et al., *Zinc-blende–wurtzite polytypism in semiconductors.* Physical Review B, 1992. **46**(16): p. 10086-10097.
77. Ikejiri, K., et al., *Zinc Blende and Wurtzite Crystal Phase Mixing and Transition in Indium Phosphide Nanowires.* Nano Letters, 2011. **11**(10): p. 4314-4318.
78. Algra, R.E., et al., *Twinning superlattices in indium phosphide nanowires.* Nature, 2008. **456**(7220): p. 369-372.
79. Glas, F., Harmand, J.C., and Patriarche, G., *Why Does Wurtzite Form in Nanowires of III-V Zinc Blende Semiconductors?* Physical Review Letters, 2007. **99**(14): p. 4.

80. Dubrovskii, V.G., et al., *Growth kinetics and crystal structure of semiconductor nanowires.* Physical Review B, 2008. **78**(23): p. 10.
81. Joyce, H.J., et al., *Phase Perfection in Zinc Blende and Wurtzite III–V Nanowires Using Basic Growth Parameters.* Nano Letters, 2010. **10**(3): p. 908-915.
82. Lehmann, S., et al., *A General Approach for Sharp Crystal Phase Switching in InAs, GaAs, InP, and GaP Nanowires Using Only Group V Flow.* Nano Letters, 2013. **13**(9): p. 4099-4105.
83. Dheeraj, D.L., et al., *Controlling crystal phases in GaAs nanowires grown by Au-assisted molecular beam epitaxy.* Nanotechnology, 2013. **24**(1): p. 015601.
84. Jacobsson, D., et al., *Interface dynamics and crystal phase switching in GaAs nanowires.* Nature, 2016. **531**(7594): p. 317-322.
85. Dubrovskii, V.G., *Development of Growth Theory for Vapor–Liquid–Solid Nanowires: Contact Angle, Truncated Facets, and Crystal Phase.* Crystal Growth & Design, 2017. **17**(5): p. 2544-2548.
86. Wallentin, J., et al., *Changes in Contact Angle of Seed Particle Correlated with Increased Zincblende Formation in Doped InP Nanowires.* Nano Letters, 2010. **10**(12): p. 4807-4812.
87. Algra, R.E., et al., *The Role of Surface Energies and Chemical Potential during Nanowire Growth.* Nano Letters, 2011. **11**(3): p. 1259-1264.
88. De, A. and Pryor, C.E., *Predicted band structures of III-V semiconductors in the wurtzite phase.* Physical Review B, 2010. **81**(15).
89. Glas, F., *Critical dimensions for the plastic relaxation of strained axial heterostructures in free-standing nanowires.* Physical Review B, 2006. **74**(12).
90. Inada, T. and Fukuda, T., *Chapter 3 Direct Synthesis and Growth of Indium Phosphide by the Liquid Phosphorus Encapsulated Czochralski Method*, in *Semiconductors and Semimetals*, R.K. Willardson and A.C. Beer, Editors. 1990, Elsevier. p. 71-92.
91. Duan, X.F. and Lieber, C.M., *General Synthesis of Compound Semiconductor Nanowires.* Advanced Materials, 2000. **12**(4): p. 298-302.
92. Duan, X.F., et al., *Indium phosphide nanowires as building blocks for nanoscale electronic and optoelectronic devices.* Nature, 2001. **409**(6816): p. 66-69.
93. Wang, J.F., et al., *Highly Polarized Photoluminescence and Photodetection from Single Indium Phosphide Nanowires.* Science, 2001. **293**(5534): p. 1455-1457.
94. Bhunia, S., et al., *Metalorganic vapor-phase epitaxial growth and characterization of vertical InP nanowires.* Applied Physics Letters, 2003. **83**(16): p. 3371-3373.
95. Mårtensson, T., et al., *Nanowire Arrays Defined by Nanoimprint Lithography.* Nano Letters, 2004. **4**(4): p. 699-702.
96. Mattila, M., et al., *Crystal-structure-dependent photoluminescence from InP nanowires.* Nanotechnology, 2006. **17**(6): p. 1580-1583.
97. Joyce, H.J., et al., *Ultralow Surface Recombination Velocity in InP Nanowires Probed by Terahertz Spectroscopy.* Nano Letters, 2012. **12**(10): p. 5325-5330.
98. Joyce, H.J., et al., *Electronic properties of GaAs, InAs and InP nanowires studied by terahertz spectroscopy.* Nanotechnology, 2013. **24**(21): p. 214006.
99. Yamaguchi, K., Itagaki, K., and Chang, Y.A., *Thermodynamic analysis of the In-P, Ga-As, In-As and Al-Sb Systems.* Calphad, 1996. **20**(4): p. 439-446.

100. Okamoto, H. and Massalski, T.B., *The Au–P (Gold-phosphorus) system.* Bulletin of Alloy Phase Diagrams, 1984. **5**(5): p. 490-491.
101. R., H.S.E. and William, H.-R., *The equilibrium diagram of the system gold-indium.* Proceedings of the Royal Society of London. Series A. Mathematical and Physical Sciences, 1964. **282**(1390): p. 318-330.
102. Persson, A.I., et al., *$InAs_{1-x}P_x$ Nanowires for Device Engineering.* Nano Letters, 2006. **6**(3): p. 403-407.
103. Ghasemi, M., Leshchenko, E.D., and Johansson, J., *Assembling your nanowire: an overview of composition tuning in ternary III–V nanowires.* Nanotechnology, 2021. **32**(7): p. 072001.
104. Merle, P., et al., *Conduction band structure of GaInP.* Physical Review B, 1977. **15**(4): p. 2032-2047.
105. Assali, S., et al., *Direct Band Gap Wurtzite Gallium Phosphide Nanowires.* Nano Letters, 2013. **13**(4): p. 1559-1563.
106. Ishida, K., et al., *Miscibility Gaps in the GaP–InP, GaP–GaSb, InP–InSn and InAs–InSb Systems.* Journal of the Less-Common Metals, 1989. **155**(2): p. 193-206.
107. Ghasemi, M., et al., *The thermodynamic assessment of the Au–In–Ga system.* Journal of Alloys and Compounds, 2014. **600**: p. 178-185.
108. Wallentin, J. and Borgström, M.T., *Doping of semiconductor nanowires.* Journal of Materials Research, 2011. **26**(17): p. 2142-2156.
109. Kim, W., et al., *Doping challenges and pathways to industrial scalability of III–V nanowire arrays.* Applied Physics Reviews, 2021. **8**(1).
110. Hijazi, H., et al., *Si Doping of Vapor–Liquid–Solid GaAs Nanowires: n-Type or p-Type?* Nano Letters, 2019. **19**(7): p. 4498-4504.
111. Kang, Y., et al., *Si doping-induced phase control, formation of p-type and n-type GaAs nanowires.* Vacuum, 2022. **195**.
112. Goto, H., et al., *Growth of Core–Shell InP Nanowires for Photovoltaic Application by Selective-Area Metal Organic Vapor Phase Epitaxy.* Applied Physics Express, 2009. **2**(3).
113. Gutsche, C., et al., *Controllable p-type doping of GaAs nanowires during vapor-liquid-solid growth.* Journal of Applied Physics, 2009. **105**(2).
114. van Weert, M.H.M., et al., *Zinc Incorporation via the Vapor–Liquid–Solid Mechanism into InP Nanowires.* Journal of the American Chemical Society, 2009. **131**(13): p. 4578–4579.
115. Borgström, M.T., et al., *Precursor evaluation for in situ InP nanowire doping.* Nanotechnology, 2008. **19**(44): p. 445602.
116. Mariani, G., et al., *GaAs nanopillar-array solar cells employing in situ surface passivation.* Nature Communications, 2013. **4**: p. 1497.
117. Qian, F., et al., *Gallium Nitride-Based Nanowire Radial Heterostructures for Nanophotonics.* Nano Letters, 2004. **4**(10): p. 1975-1979.
118. Astromskas, G., et al., *Doping Incorporation in InAs nanowires characterized by capacitance measurements.* Journal of Applied Physics, 2010. **108**(5).
119. Gutsche, C., et al., *n-Type Doping of Vapor–Liquid–Solid Grown GaAs Nanowires.* Nanoscale Research Letters, 2011. **6**(1): p. 65.
120. Minot, E.D., et al., *Single Quantum Dot Nanowire LEDs.* Nano Letters, 2007. **7**(2): p. 367-371.

121. Hirt, G., et al., *Compensation Mechanisms in Nominally Undoped Semiinsulating InP and Comparison with Undoped InP Grown under Stoichiometry Control.* Journal of Electronic Materials, 1991. **20**(12): p. 1065-1068.
122. Temkin, H., Dutt, B.V., and Bonner, W.A., *Photoluminescence study of native defects in InP.* Applied Physics Letters, 1981. **38**(6): p. 431-433.
123. Carlson, D.E. and Wronski, C.R., *Amorphous silicon solar cell.* Applied Physics Letters, 1976. **28**(11): p. 671-673.
124. Otnes, G., et al., *Understanding InP Nanowire Array Solar Cell Performance by Nanoprobe-Enabled Single Nanowire Measurements.* Nano Letters, 2018. **18**(5): p. 3038-3046.
125. Borgström, M.T., et al., *In situ etching for total control over axial and radial nanowire growth.* Nano Research, 2010. **3**(4): p. 264-270.
126. Storm, K., et al., *Spatially resolved Hall effect measurement in a single semiconductor nanowire.* Nature Nanotechnology, 2012. 7(11): p. 718-722.
127. Blomers, C., et al., *Hall effect measurements on InAs nanowires.* Applied Physics Letters, 2012. **101**(15).
128. Troian, A., et al., *Nanobeam X-ray Fluorescence Dopant Mapping Reveals Dynamics of in Situ Zn-Doping in Nanowires.* Nano Letters, 2018. **18**(10): p. 6461-6468.
129. Berg, A., et al., *In situ etching for control over axial and radial III-V nanowire growth rates using HBr.* Nanotechnology, 2014. **25**(50).
130. Su, X., et al., *Effect of hydrogen chloride etching on carrier recombination processes of indium phosphide nanowires.* Nanoscale, 2019. **11**(40): p. 18550-18558.
131. Cui, Y., et al., *Diameter-controlled synthesis of single-crystal silicon nanowires.* Applied Physics Letters, 2001. **78**(15): p. 2214-2216.
132. Guo, L.J., *Nanoimprint Lithography: Methods and Material Requirements.* Advanced Materials, 2007. **19**(4): p. 495-513.
133. Solak, H.H., Dais, C., and Clube, F., *Displacement Talbot lithography: a new method for high-resolution patterning of large areas.* Optics Express, 2011. **19**(11): p. 10686-10691.
134. Coulon, P.M., et al., *Displacement Talbot lithography for nano-engineering of III-nitride materials.* Microsystems & Nanoengineering, 2019. **5**: p. 52.
135. Gomez, V.J., et al., *Wafer-scale nanofabrication of sub-100 nm arrays by deep-UV displacement Talbot lithography.* Nanotechnology, 2020. **31**(29): p. 295301.
136. Gallet, D., et al., *Protection of InP EPI-Ready Wafers by Controlled Oxide Growth.* Journal of Electronic Materials, 1991. **20**(12): p. 963-965.
137. Allwood, D.A., et al., *Monitoring epiready semiconductor wafers.* Thin Solid Films, 2002. **412**(1-2): p. 76-83.
138. Pierret, A., et al., *Generic nano-imprint process for fabrication of nanowire arrays.* Nanotechnology, 2010. **21**(6): p. 065305.
139. Tchernycheva, M., et al., *Temperature conditions for GaAs nanowire formation by Au-assisted molecular beam epitaxy.* Nanotechnology, 2006. **17**(16): p. 4025-4030.
140. Whiticar, A.M., et al., *Annealing of Au, Ag and Au-Ag alloy nanoparticle arrays on GaAs (100) and (111)B.* Nanotechnology, 2017. **28**(20): p. 12.
141. Otnes, G., et al., *Strategies to obtain pattern fidelity in nanowire growth from large-area surfaces patterned using nanoimprint lithography.* Nano Research, 2016. **9**(10): p. 2852-2861.

142. Åberg, I., et al., *A GaAs Nanowire Array Solar Cell With 15.3% Efficiency at 1 Sun.* IEEE Journal of Photovoltaics, 2016. **6**(1): p. 185-190.
143. Zeng, X., et al., *In situ passivation of $GaxIn_{(1-x)}P$ nanowires using radial $Al_yIn_{(1-y)}P$ shells grown by MOVPE.* Nanotechnology, 2021. **32**(42).
144. Montazeri, M., et al., *Direct Measure of Strain and Electronic Structure in GaAs/GaP Core–Shell Nanowires.* Nano Letters, 2010. **10**(3): p. 880-886.
145. Liu, P.B., et al., *Core–shell nanowire diode based on strain-engineered bandgap.* Physica Status Solidi A, 2015. **212**(3): p. 617-622.
146. Spirkoska, D., et al., *Free standing modulation doped core-shell GaAs/AlGaAs hetero-nanowires.* Physica Status Solidi-Rapid Research Letters, 2011. **5**(9): p. 353-355.
147. Jadczak, J., et al., *Unintentional High-Density p-Type Modulation Doping of a GaAs/AlAs Core–Multishell Nanowire.* Nano Letters, 2014. **14**(5): p. 2807-2814.
148. Boland, J.L., et al., *Modulation Doping of GaAs/AlGaAs Core–Shell Nanowires With Effective Defect Passivation and High Electron Mobility.* Nano Letters, 2015. **15**(2): p. 1336-1342.
149. Saket, O., et al., *Influence of surface passivation on the electrical properties of p–i–n GaAsP nanowires.* Applied Physics Letters, 2020. **117**(12).
150. Yablonovitch, E., et al., *Unusually Low Surface-Recombination Velocity on Silicon and Germanium Surfaces.* Physical Review Letters, 1986. **57**(2): p. 249-252.
151. Bessolov, V.N. and Lebedev, M.V., *Chalcogenide passivation of III–V semiconductor surfaces.* Semiconductors, 1998. **32**(11): p. 1141-1156.
152. Tajik, N., Haapamaki, C.M., and LaPierre, R.R., *Photoluminescence model of sulfur passivated p-InP nanowires.* Nanotechnology, 2012. **23**(31): p. 315703.
153. van Vugt, L.K., et al., *Increase of the Photoluminescence Intensity of InP Nanowires by Photoassisted Surface Passivation.* Journal of the American Chemical Society, 2005. **127**(35): p. 12357-12362.
154. Gutsche, C., et al., *Direct Determination of Minority Carrier Diffusion Lengths at Axial GaAs Nanowire p–n Junctions.* Nano Letters, 2012. **12**(3): p. 1453-1458.
155. Gocalinska, A., Rubini, S., and Pelucchi, E., *Native oxides formation and surface wettability of epitaxial III–V materials: The case of InP and GaAs.* Applied Surface Science, 2016. **383**: p. 19-27.
156. Higuera-Rodriguez, A., et al., *Ultralow Surface Recombination Velocity in Passivated InGaAs/InP Nanopillars.* Nano Letters, 2017. **17**(4): p. 2627-2633.
157. Min, B.D., et al., *Semiconductor Nanowires Surrounded by Cylindrical Al_2O_3 Shells.* Journal of Electronic Materials, 2003. **32**(11): p. 1344-1348.
158. Fronheiser, J., Balch, J., and Tsakalakos, L., *Conformal dielectric films on silicon nanowire arrays by plasma enhanced chemical vapor deposition.* Journal of Nanoparticle Research, 2008. **10**(6): p. 955-963.
159. Black, L.E., et al., *Effective Surface Passivation of InP Nanowires by Atomic-Layer-Deposited Al_2O_3 with PO_x Interlaye.* Nano Letters, 2017. **17**(10): p. 6287-6294.
160. Münch, S., et al., *Time-resolved photoluminescence investigations on HfO_2-capped InP nanowires.* Nanotechnology, 2010. **21**(10): p. 105711.
161. Dhaka, V., et al., *Protective capping and surface passivation of III-V nanowires by atomic layer deposition.* AIP Advances, 2016. **6**(1).

162. Mallorquí, A.D., et al., *Field-effect passivation on silicon nanowire solar cells.* Nano Research, 2014. **8**(2): p. 673-681.
163. Murotani, H., et al., *Effects of exciton localization on internal quantum efficiency of InGaN nanowires.* Journal of Applied Physics, 2013. **114**(15).
164. Zhang, W., et al., *Recombination dynamics in aerotaxy-grown Zn-doped GaAs nanowires.* Nanotechnology, 2016. **27**(45): p. 455704.
165. Hochbaum, A.I. and Yang, P.D., *Semiconductor Nanowires for Energy Conversion.* Chemical Reviews, 2010. **110**(1): p. 527-546.
166. Haverkort, J.E.M., Garnett, E.C., and Bakkers, E.P.A.M., *Fundamentals of the nanowire solar cell: Optimization of the open circuit voltage.* Applied Physics Reviews, 2018. **5**(3).
167. Wallentin, J., et al., *InP Nanowire Array Solar Cells Achieving 13.8% Efficiency by Exceeding the Ray Optics Limit.* Science, 2013. **339**(6123): p. 1057-1060.
168. Cui, Y.C., et al., *Efficiency Enhancement of InP Nanowire Solar Cells by Surface Cleaning.* Nano Letters, 2013. **13**(9): p. 4113-4117.
169. van Dam, D., et al., *High-Efficiency Nanowire Solar Cells with Omnidirectionally Enhanced Absorption Due to Self-Aligned Indium–Tin–Oxide Mie Scatterers.* ACS Nano, 2016. **10**(12): p. 11414-11419.
170. Oener, S.Z., et al., *Charge carrier-selective contacts for nanowire solar cells.* Nature Communications, 2018. **9**(1): p. 3248.
171. Raj, V., Tan, H.H., and Jagadish, C., *Non-epitaxial carrier selective contacts for III-V solar cells: A review.* Applied Materials Today, 2020. **18**.
172. Sze, S.M., *Semiconductor Devices: Physics and Technology*. 2012: John Wiley & Sons Singapore Pte. Limited.
173. Raj, V., Tan, H., and Jagadish, C., *Axial vs radial junction nanowire solar cell.* AJP Reports, 2019. **28**: p. 719-746.
174. Tian, B., et al., *Coaxial silicon nanowires as solar cells and nanoelectronic power sources.* Nature, 2007. **449**(7164): p. 885-889.
175. LaPierre, R.R., *Numerical model of current-voltage characteristics and efficiency of GaAs nanowire solar cells.* Journal of Applied Physics, 2011. **109**(3).
176. Wang, S.J., et al., *Axially connected nanowire core-shell p-n junctions: a composite structure for high-efficiency solar cells.* Nanoscale Research Letters, 2015. **10**.
177. Perkins, J.H., et al., *Pt and Zn based ohmic contacts to p-type InP*, in *Proceedings of 1994 IEEE 6th International Conference on Indium Phosphide and Related Materials (IPRM)*. 1994. p. 190-193.
178. Timm, R., et al., *Current–Voltage Characterization of Individual As-Grown Nanowires Using a Scanning Tunneling Microscope.* Nano Letters, 2013. **13**(11): p. 5182-5189.
179. Holmer, J., et al., *An STM – SEM setup for characterizing photon and electron induced effects in single photovoltaic nanowires.* Nano Energy, 2018. **53**: p. 175-181.
180. Kleindiek, S., et al., *Miniature three-axis micropositioner for scanning proximal probe and other applications.* Journal of Vacuum Science & Technology B, 1995. **13**(6): p. 2653-2656.
181. Erlandsson, R. and Olsson, L., *A three-axis micropositioner for ultrahigh vacuum use based on the inertial slider principle.* Review of Scientific Instruments, 1996. **67**(4): p. 1472-1474.

182. Yu, S., Roemer, F., and Witzigmann, B., *Analysis of surface recombination in nanowire array solar cells.* Journal of Photonics for Energy, 2012. **2**(1).
183. Schmitt, S.W., et al., *Probing photo-carrier collection efficiencies of individual silicon nanowire diodes on a wafer substrate.* Nanoscale, 2014. **6**(14): p. 7897-902.
184. Hanoka, J.I. and Bell, R.O., *Electron-Beam-Induced Currents in Semiconductors.* Annual Review of Materials Science, 1981. **11**: p. 353-380.
185. Leamy, H.J., *Charge collection scanning electron microscopy.* Journal of Applied Physics, 1982. **53**(6): p. R51-R80.
186. Gustafsson, A., Björk, M.T., and Samuelson, L., *Locating nanowire heterostructures by electron beam induced current.* Nanotechnology, 2007. **18**(20).
187. Chang, C.C., et al., *Electrical and Optical Characterization of Surface Passivation in GaAs Nanowires.* Nano Letters, 2012. **12**(9): p. 4484-4489.
188. Chen, C.Y., et al., *Electron beam induced current in InSb-InAs nanowire type-III heterostructures.* Applied Physics Letters, 2012. **101**(6).
189. Chen, G.N., et al., *Subsurface Imaging of Coupled Carrier Transport in GaAs/AlGaAs Core–Shell Nanowires.* Nano Letters, 2015. **15**(1): p. 75-79.
190. Zhong, Z., et al., *Efficiency enhancement of axial junction InP single nanowire solar cells by dielectric coating.* Nano Energy, 2016. **28**: p. 106-114.
191. Fast, J., et al., *Hot-carrier separation in heterostructure nanowires observed by electron-beam induced current.* Nanotechnology, 2020. **31**(39).
192. Katzenmeyer, A.M., et al., *Poole–Frenkel Effect and Phonon-Assisted Tunneling in GaAs Nanowires.* Nano Letters, 2010. **10**(12): p. 4935-4938.
193. Talin, A.A., et al., *Transport characterization in nanowires using an electrical nanoprobe.* Semiconductor Science and Technology, 2010. **25**(2).
194. Arstila, K., et al., *Nanoprober-based EBIC measurements for nanowire transistor structures.* Microelectronic Engineering, 2013. **105**: p. 99-102.
195. Zhao, S., et al., *Probing the electrical transport properties of intrinsic InN nanowires.* Applied Physics Letters, 2013. **102**(7).
196. Piazza, V., et al., *Nanoscale analysis of electrical junctions in InGaP nanowires grown by template-assisted selective epitaxy.* Applied Physics Letters, 2019. **114**(10).
197. Yang, M.Z., et al., *Axial EBIC oscillations at core/shell GaAs/Fe nanowire contacts.* Nanotechnology, 2019. **30**(2): p. 025701.
198. Saket, O., et al., *Nanoscale electrical analyses of axial-junction GaAsP nanowires for solar cell applications.* Nanotechnology, 2020. **31**(14): p. 145708.
199. Saket, O., et al., *Investigation of the effect of the doping order in GaN nanowire p–n junctions grown by molecular-beam epitaxy.* Nanotechnology, 2021. **32**(8): p. 085705.
200. Christesen, J.D., et al., *Design Principles for Photovoltaic Devices Based on Si Nanowires with Axial or Radial p–n Junctions.* Nano Letters, 2012. **12**(11): p. 6024-6029.
201. Chen, Y., et al., *Optimization of the short-circuit current in an InP nanowire array solar cell through opto-electronic modeling.* Nanotechnology, 2016. **27**(43): p. 435404.
202. Shockley, W. and Queisser, H.J., *Detailed Balance Limit of Efficiency of p-n Junction Solar Cells.* Journal of Applied Physics, 1961. **32**(3): p. 510-519.
203. Peters, I.M. and Buonassisi, T., *Energy Yield Limits for Single-Junction Solar Cells.* Joule, 2018. **2**(6): p. 1160-1170.

204. Hirst, L.C. and Ekins-Daukes, N.J., *Fundamental losses in solar cells.* Progress in Photovoltaics: Research and Applications, 2011. **19**(3): p. 286-293.
205. *Tables for Reference Solar Spectral Irradiances: Direct Normal and Hemispherical on 37° Tilted Surface.* . ASTM International.
206. Vos, A.D., *Detailed balance limit of the efficiency of tandem solar cells.* Journal of Physics D: Applied Physics, 1980. **13**(5): p. 839-846.
207. Esaki, L., *New Phenomenon in Narrow Germanium p–n Junctions.* Physical Review, 1958. **109**(2): p. 603-604.
208. Hall, R.N., *Tunnel Diodes.* IRE Transactions on Electron Devices, 1960. 7(1): p. 1-9.
209. Sze, S.M. and Ng, K.K., *Physics of Semiconductor Devices*. 2006.
210. Guter, W. and Bett, A.W. *IV-Characterization of Devices Consisting of Solar Cells and Tunnel Diodes*. in *2006 IEEE 4th World Conference on Photovoltaic Energy Conference*. 2006.
211. Wallentin, J., et al., *High-Performance Single Nanowire Tunnel Diodes.* Nano Letters, 2010. **10**(3): p. 974-979.
212. Björk, M.T., et al., *Si–InAs heterojunction Esaki tunnel diodes with high current densities.* Applied Physics Letters, 2010. **97**(16).
213. Fung, W.Y., Chen, L., and Lu, W., *Esaki tunnel diodes based on vertical Si-Ge nanowire heterojunctions.* Applied Physics Letters, 2011. **99**(9).
214. Ganjipour, B., et al., *High Current Density Esaki Tunnel Diodes Based on GaSb-InAsSb Heterostructure Nanowires.* Nano Letters, 2011. **11**(10): p. 4222-4226.
215. Dey, A.W., et al., *Combining Axial and Radial Nanowire Heterostructures: Radial Esaki Diodes and Tunnel Field-Effect Transistors.* Nano Letters, 2013. **13**(12): p. 5919-5924.
216. Zeng, X., et al., *InP/GaInP nanowire tunnel diodes.* Nano Research, 2018. **11**(5): p. 2523-2531.
217. Tizno, O., et al., *Radial tunnel diodes based on InP/InGaAs core-shell nanowires.* Applied Physics Letters, 2017. **110**(11).
218. Ra, Y.H. and Lee, C.R., *Core–Shell Tunnel Junction Nanowire White-Light-Emitting Diode.* Nano Letters, 2020. **20**(6): p. 4162-4168.
219. Fossum, J.G., *Physical Operation of Back-Surface-Field Silicon Solar-Cells.* IEEE Transactions on Electron Devices, 1977. **24**(4): p. 322-325.
220. Barrigón, E., et al., *Implications of low breakdown voltage of component subcells on external quantum efficiency measurements of multijunction solar cells.* Progress in Photovoltaics: Research and Applications, 2015. **23**(11): p. 1597-1607.
221. Romero, M.J., Olson, J.M., and Al-Jassim, M.M. *Light-Biasing Electron-Beam-Induced-Current Measurements for Multijunction Solar Cells: Preprint*. 2001. United States.
222. Maximenko, S.I., et al., *Application of CL/EBIC-SEM Techniques for Characterization of Radiation Effects in Multijunction Solar Cells.* IEEE Transactions on Nuclear Science, 2010. **57**(6): p. 3095-3100.
223. LaPierre, R.R., *Theoretical conversion efficiency of a two-junction III-V nanowire on Si solar cell.* Journal of Applied Physics, 2011. **110**(1).
224. VanSant, K.T., Tamboli, A.C., and Warren, E.L., *III-V-on-Si Tandem Solar Cells.* Joule, 2021. **5**(3): p. 514-518.

225. Yao, M.Q., et al., *Tandem Solar Cells Using GaAs Nanowires on Si: Design, Fabrication, and Observation of Voltage Addition.* Nano Letters, 2015. **15**(11): p. 7217-7224.
226. Heurlin, M., et al., *Continuous gas-phase synthesis of nanowires with tunable properties.* Nature, 2012. **492**(7427): p. 90-94.
227. Alcott, G., *Nanowire Growth System Having Nanoparticles Aerosols Generator*. 2016, Sol Voltaics AB: US.
228. Mårtensson, N. and Castillo Leon, J., *Method For Transferring Nanowires From A Fluid To A Substrate Surface*. 2017, Sol Voltaics AB: EP.
229. Olson Jerry, M., *Multi-Junction Photovoltaic Cell With Nanowires*. 2012, Sol Voltaics AB: EP.
230. Björk, M., et al., *Dual Layer Photovoltaic Device*. 2016, Sol Voltaics AB: WO.
231. Zhang, S., et al., *Highly flexible radial tandem junction thin film solar cells with excellent power-to-weight ratio.* Nano Energy, 2021. **86**.
232. Kempa, T.J., et al., *Single and Tandem Axial p-i-n Nanowire Photovoltaic Devices.* Nano Letters, 2008. **8**(10): p. 3456-3460.
233. Heurlin, M., et al., *Axial InP Nanowire Tandem Junction Grown on a Silicon Substrate.* Nano Letters, 2011. **11**(5): p. 2028-2031.
234. Black, L.E. and Kessels, W.M.M., *PO_x/Al_2O_3 stacks: Highly effective surface passivation of crystalline silicon with a large positive fixed charge.* Applied Physics Letters, 2018. **112**(20).
235. Battaglia, C., et al., *Hole Selective MoO_x Contact for Silicon Solar Cells.* Nano Letters, 2014. **14**(2): p. 967-971.
236. Bivour, M., et al., *Molybdenum and tungsten oxide: High work function wide band gap contact materials for hole selective contacts of silicon solar cells.* Solar Energy Materials and Solar Cells, 2015. **142**: p. 34-41.
237. Dang, H.M. and Singh, V.P., *Nanowire CdS-CdTe Solar Cells with Molybdenum Oxide as Contact.* Scientific Reports, 2015. **5**.
238. Geissbuhler, J., et al., *22.5% efficient silicon heterojunction solar cell with molybdenum oxide hole collector.* Applied Physics Letters, 2015. **107**(8).
239. Essig, S., et al., *Toward Annealing-Stable Molybdenum-Oxide-Based Hole-Selective Contacts For Silicon Photovoltaics.* Solar Rrl, 2018. **2**(4): p. 5.
240. Ivarsson, E., *Molybdenum Oxide as a Selective Hole Electrical Contact for Indium Phosphide Nanowires*, in *Solid State Physics*. 2021, Lund University.
241. Spurgeon, J.M., et al., *Repeated epitaxial growth and transfer of arrays of patterned, vertically aligned, crystalline Si wires from a single Si(111) substrate.* Applied Physics Letters, 2008. **93**(3).
242. Plass, K.E., et al., *Flexible Polymer-Embedded Si Wire Arrays.* Advanced Materials, 2009. **21**(3): p. 325-328.
243. Weisse, J.M., et al., *Fabrication of Flexible and Vertical Silicon Nanowire Electronics.* Nano Letters, 2012. **12**(6): p. 3339-3343.
244. Cavalli, A., et al., *Nanowire polymer transfer for enhanced solar cell performance and lower cost.* Nano-Structures & Nano-Objects, 2018. **16**: p. 59-62.
245. Jafari Jam, R., et al., *Embedded sacrificial AlAs segments in GaAs nanowires for substrate reuse.* Nanotechnology, 2020. **31**(20): p. 204002.

246. Flatt, P., *AlP sacrificial layer for GaP NW growth*, in *Solid State Physics*. 2020 Lund University.

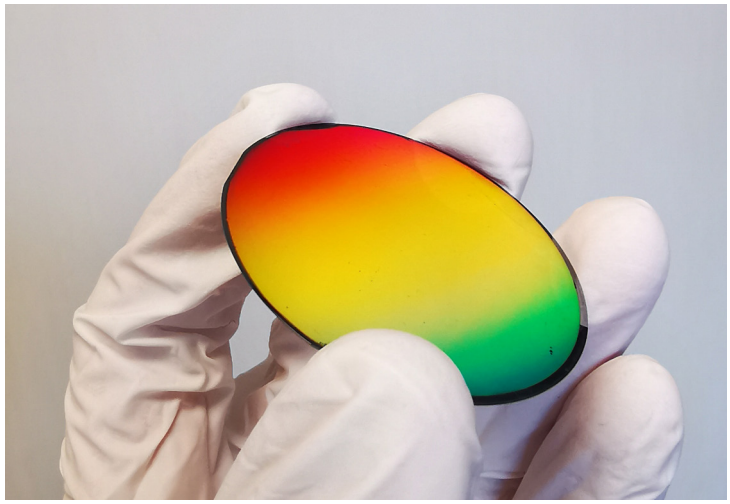

This thesis describes the epitaxial growth and subsequent characterization of photovoltaic nanowires. Solar cells depend on large areas to convert sunlight to electricity. The photograph above demonstrates a wafer-scale array of nanowires.

Printed by Media-Tryck, Lund 2022 NORDIC SWAN ECOLABEL 3041 0903

LUND UNIVERSITY

Division of Solid State Physics
Department of Physics
Faculty of Engineering
Lund University

ISBN 978-91-8039-209-9